Materials Today Bio 23 (2023) 100850

Contents lists available at ScienceDirect

Materials Today Bio

journal homepage: www.journals.elsevier.com/materials-today-bio

Bioinspired extracellular vesicle-coated silica nanoparticles as selective delivery systems

Bianca Dumontel [a,1], Carla Jiménez-Jiménez [a,b,1], María Vallet-Regí [a,b,*], Miguel Manzano [a,b,**]

[a] Department of Chemistry in Pharmaceutical Sciences, School of Pharmacy, Institute Hospital 12 de Octubre (imas12), Universidad Complutense de Madrid, UCM, Madrid, 28040, Spain
[b] Networking Research Center on Bioengineering, Biomaterials and Nanomedicine (CIBER-BBN), Madrid, 28029, Spain

ARTICLE INFO

Keywords:
Nanoparticles
Extracellular vesicles
Bioinspired nanocarriers
Selective targeting

ABSTRACT

In recent years, there has been a breakthrough in the integration of artificial nanoplatforms with natural biomaterials for the development of more efficient drug delivery systems. The formulation of bioinspired nanosystems, combining the benefits of synthetic nanoparticles with the natural features of biological materials, provides an efficient strategy to improve nanoparticle circulation time, biocompatibility and specificity toward targeted tissues. Among others biological materials, extracellular vesicles (EVs), membranous structures secreted by many types of cells composed by a protein rich lipid bilayer, have shown a great potential as drug delivery systems themselves and in combination with artificial nanoparticles. The reason for such interest relays on their natural properties, such as overcoming several biological barriers or migration towards specific tissues. Here, we propose the use of mesoporous silica nanoparticles (MSNs) as efficient and versatile nanocarriers in combination with tumor derived extracellular vesicles (EVs) for the development of selective drug delivery systems. The hybrid nanosystems demonstrated selective cellular internalization in parent cells, indicating that the EV targeting capabilities were efficiently transferred to MSNs by the developed coating strategy. As a result, EVs-coated MSNs provided an enhanced and selective intracellular accumulation of doxorubicin and a specific cytotoxic activity against targeted cancer cells, revealing these hybrid nanosystems as promising candidates for the development of targeted treatments.

In the last few years, nanotechnology has focused on the development of cancer therapeutics that might offer new solutions in terms of efficacy and safety [1]. In this sense, nanotechnology has demonstrated to be useful for overcoming some limitations of conventional therapies, such as certain biological barriers, either systemic, microenvironmental or cellular [2]. Additionally, the use of nanoparticles in medicine has facilitated the solubilization, protection from degradation and sustained release of many pharmaceutical ingredients [3]. Moreover, the relatively large dimensions of nanoparticles in comparison with conventional therapeutic agents allows the incorporation of several functional components that might contribute to improve *in vivo* targeting efficiency and reduce nonspecific side effects [4].

Among the different types of nanoparticles for drug delivery applications, biologically derived nanocarriers (*e.g.*, extracellular vesicles and exosomes) and artificially engineered nanovehicles (*e.g.*, liposomes, polymer and inorganic nanoparticles) have been widely explored thanks to their outstanding features. The former natural nanoparticles exhibit high biocompatibility, stability and, therefore, long circulation time. The latter artificial nanoplatforms can be engineered to present tailored characteristics specially designed for each targeted application. However, low drug loading efficiency together with the current isolation and purification methods for biological nanocarriers production lead to heterogeneity, being expensive and presenting low yields, which might be a challenge for future large scale-up [5]. On the other hand, conventional nanoparticles present some pitfalls, such as long-term stability issues and complicated functionalization processes to achieve active

* Corresponding author. Department of Chemistry in Pharmaceutical Sciences, School of Pharmacy, Institute Hospital 12 de Octubre (imas12), Universidad Complutense de Madrid, UCM, Madrid, 28040, Spain.
** Corresponding author. Department of Chemistry in Pharmaceutical Sciences, School of Pharmacy, Institute Hospital 12 de Octubre (imas12), Universidad Complutense de Madrid, UCM, Madrid, 28040, Spain.
E-mail addresses: vallet@ucm.es (M. Vallet-Regí), mmanzano@ucm.es (M. Manzano).
[1] These authors contributed equally.

https://doi.org/10.1016/j.mtbio.2023.100850
Received 27 June 2023; Received in revised form 25 October 2023; Accepted 26 October 2023
Available online 29 October 2023

targeting towards specific tissues [6].

The combination of biological elements with artificially engineered nanoparticles has led to the development of bioinspired nanocarriers that bring the benefits from both Worlds. It is possible to develop robust and reproducible nanoparticles with long circulation times and high biocompatibility being able to reach specific solid tumor sites [7].

Among the numerous types of engineered artificial nanocarriers, mesoporous silica nanoparticles (MSNs) have caught the attention of the research community thanks to their outstanding properties for drug delivery, such as their high loading capacity, robustness and biocompatibility [8–11]. It is also relatively easy to modify their surface with a plethora of different moieties to provide them with many capabilities [12,13]. In recent biomimetic approaches, the blood circulation time and stability of MSNs have been improved by coating their surface with cell membranes from different sources, such as red blood cell membranes, white blood cells, platelets, cancer cells, mesenchymal stem cells, and beta cells, among others [14–17].

The cell membranes replicate the surface functionality of cells to improve accumulation and efficacy at the target site, fueling the development of engineered delivery systems that combine certain biomimetic features from the cell membranes with the functional versatility and loading capacity from MSNs [18]. However, maintaining all cell membrane functionalities during the isolation and manipulation processes constitutes a technical challenge. Excessive stress and physicochemical conditions during cell membrane harvesting could lead to loss or denaturation of important functional components, such as structural lipids, proteins and other components responsible for biomimicry and cellular recognition, ultimately impairing cell membrane features [19–21].

A potential alternative could be the use of extracellular vesicles (EVs) as materials for MSNs coating. EVs are lipid bilayer vesicles that are naturally secreted by the cells and play an important role in cellular communication by acting as endogenous vectors to transport biomolecules. As natural cells, EVs display proteins, ligands and targeting moieties on their surface but in general they better conserve their integrity during isolation and storage than isolated cell membranes [19,22]. Moreover, the presence of both endosomal and plasma membrane proteins in EVs was found to provide better targeting and immune evasion capabilities than cell membranes in bioinspired nanosystems based on polymeric nanoparticles [23].

In this way, it is possible to employ EVs from different sources to coat MSNs and, therefore, endow engineered nanocarriers with the ability to mimic certain processes exhibited by biological entities, such as long circulation times, selective cellular internalization or tropism towards specific targeted tissues. In particular, EVs derived from tumoral cells, which are involved in pathogenesis, modulation of tumor microenvironment and metastatic process, have shown distinct homing capabilities towards source cells, making them interesting candidates for targeted applications [24–26].

In this work, we have engineered bioinspired nanocarriers based on MSNs coated with EVs derived from two different tumoral cell lines (Scheme 1). The hybrid nanosystems were designed to combine the native homing properties of EVs toward their parent cells with the high loading and release capabilities from MSNs, which allowed killing specific cancer cells without affecting healthy cells. The selective internalization and therapeutic potential of the proposed EVs-coated MSNs were assessed *in vitro*, as a proof of concept for the formulation of promising candidates for targeted drug delivery applications.

1. Results and discussion

MSNs synthesis and coating with tumor-derived EVs. MSNs were synthesized by a modification of Stöber method [27] and their outer surface was then functionalized with amino groups to confer them a positive surface charge, aimed to promote the subsequent coating with negatively charged EVs.

The obtained MSNs presented a spherical shape and a homogeneous size of about 150 nm, as depicted by Transmission Electron Microscopy (TEM) micrograph shown in Fig. 1A and Fig. S1A (Supporting Information).

The mesoporosity of the material was analyzed by X-ray diffraction (XRD) and N_2 adsorption measurements. X-ray diffractogram (Fig. S1B) revealed the characteristic 2D hexagonal symmetry of MSNs while analysis of adsorption and desorption isotherms (Fig. S1C) confirmed their high surface area (917 m^2/g) and pore volume (0.75 cm^2/g) and the presence of mesopores with a narrow size distribution of around 2

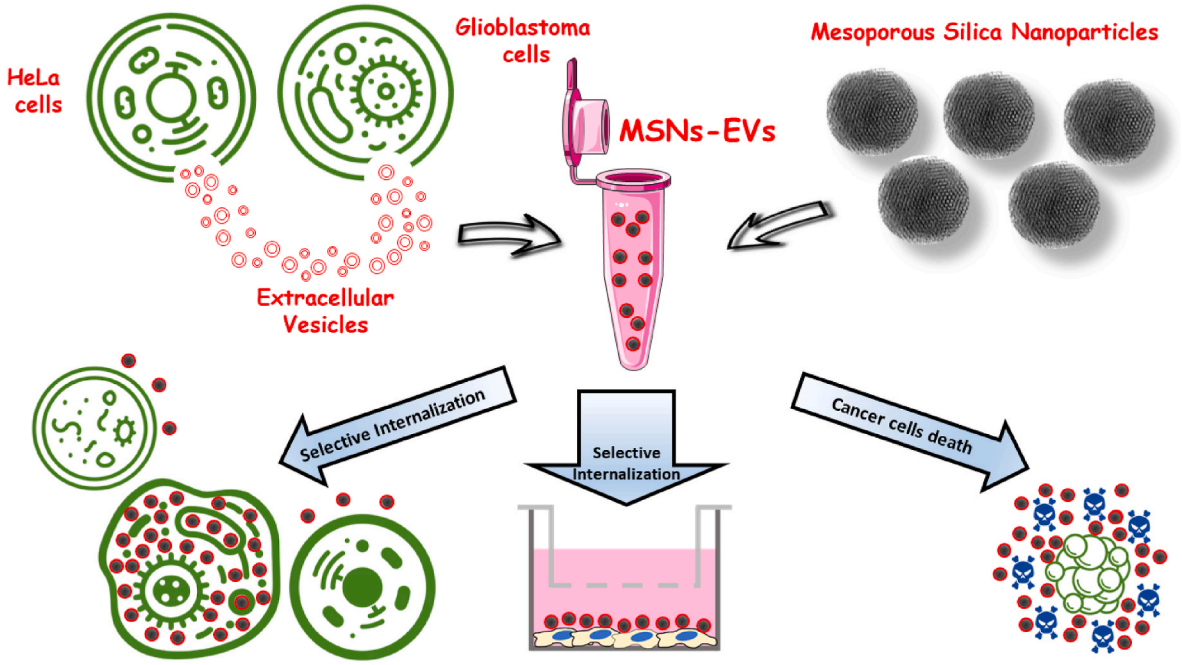

Scheme 1. Schematic representation of Mesoporous Silica Nanoparticles (MSNs) coating with Extracellular vesicles (EVs) from different sources and their evaluation for selective cellular internalization, both upon direct administration or in presence of a barrier model, and selective cancer cells death.

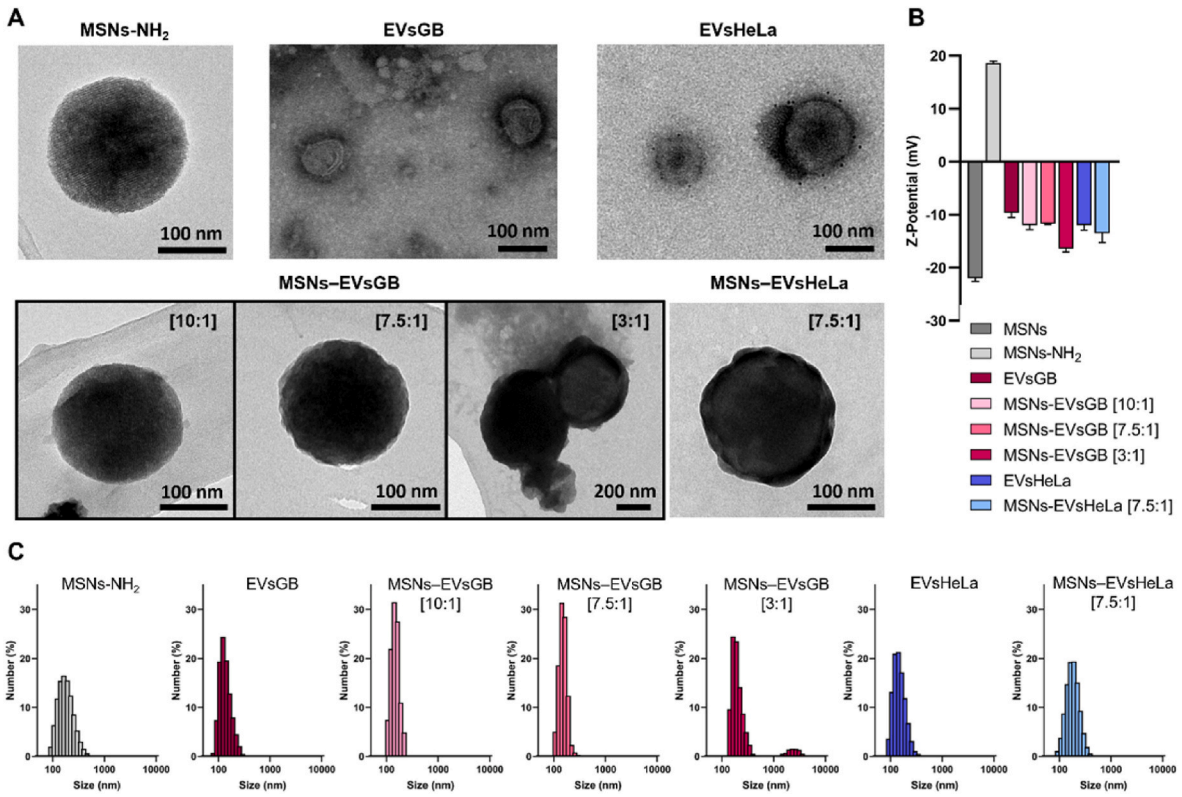

Fig. 1. Optimization of MSNs coating with tumor-derived EVs. (**A**) TEM micrographs, (**B**) Z-potential and (**C**) hydrodynamic size distribution of: pristine MSNs; amino-functionalized MSNs (MSNs-NH_2); EVs extracted from glioblastoma cells (EVsGB) and HeLa cells (EVsHeLa); MSNs coated with increasing amount of EVsGB (MSNs–EVsGB with [μg MSNs:μg EV proteins] ratios of [10:1], [7.5:1] and [3:1]); MSNs coated with EVsHeLa (MSNs–EVsHeLa [7.5:1]). For TEM analysis samples were stained with a 1 % phosphotungstic acid (PTA) solution in water. Z-Potential and hydrodynamic size distributions of EVs were measured in PBS, those of MSNs and MSNs–EVs in a 1:1 (v/v) solution of deionized water and PBS.

nm.

Fourier-transform Infrared spectroscopy (FT-IR) analyses (Fig. S1D) were performed to confirm the success of the surface chemical functionalization. Compared to as produced MSNs, the spectrum of functionalized nanoparticles showed vibration band at 1630 cm^{-1} ascribable to $–NH_2$ groups. Moreover, a strong decrease in the intensity of vibration bands from $–CH_x$ groups was observed, indicating the efficient removal of CTAB pore directing agent during the final step of the synthesis procedure. The residual weak bands from alkyl groups were attributed to the aminopropylsilane molecules used as functionalizing agent. The functionalization of MSNs surface was also confirmed by Z-Potential measurements. Unmodified silica nanoparticles were characterized by a negative surface charge from the silanol groups, while functionalized MSNs-NH_2 presented a positive Z-potential confirming the presence of positive amino groups on their surface (Fig. 1B and Table 1).

Amino-functionalized MSNs (referred to as MSNs for brevity) were combined with tumor-derived EVs to obtain hybrid nanosystems formed by a mesoporous silica core shielded by an EV coating layer.

EVs were extracted from conditioned media of two cancerous cell lines, *i.e.* a glioblastoma cell line (HGUE-GB-39) and a cervical cancer cell line (HeLa). The size, shape and morphology of both EVsGB and EVsHeLa were analyzed by TEM with phosphotungstic acid negative staining, showing the presence of round structures with the characteristic cup-shape morphology of stained EVs and diameter of about 100 nm (Fig. 1A). Sample size was also confirmed by DLS measurements, which showed monomodal size distributions with mean hydrodynamic diameters of *ca.* 120 and 140 nm for EVsGB and EVsHeLa, respectively (Fig. 1C and Table 1). Finally, Z-Potential were measured obtaining negative values for both types of EVs (Fig. 1B and Table 1), in agreement with the literature [28].

EVs extracted from glioblastoma cells were co-incubated with amino-functionalized MSNs at different ratios to optimize the coating efficiency. In particular, ratios of 10:1, 7.5:1 and 3:1 of μg of MSNs:μg of EV (protein content) were tested.

TEM micrographs with staining allowed to assess the correct coating of the silica surface. Indeed, while the porous mesostructure was clearly visible in the uncoated MSNs, it was hidden in MSNs–EVsGB samples (Fig. 1A). Coated MSNs appeared surrounded by a dark layer of stained

Table 1
Z-potential values and mean hydrodynamic diameter of DLS measurements presented in Fig. 1B and C. Amounts of EVs associated with MSNs and remaining in solution at the end of the coating process using different amount of EVs derived from glioblastoma cells (MSNs–EVsGB with [μg MSNs:μg EV proteins] ratios of [10:1], [7.5:1] and [3:1]) and the optimized amount of EVs derived from HeLa cells (MSNs–EVsHeLa [7.5:1]). EV amounts are expressed as μg of proteins, measured by microBCA protein assay.

	MSNs	MSNs-NH_2	EVsGB	MSNs-EVsGB$_{[10:1]}$	MSNs-EVsGB$_{[7.5:1]}$	MSNs-EVsGB$_{[3:1]}$	EVsHeLa	MSNs-EVsHeLa$_{[7.5:1]}$
Z-Potential (mV)	−22	+18.6	−9.6	−12	−11.7	−16.4	−12	−13.5
Size (nm)	142	164	122	142	142	164/2000	142	164
μg EVs associated (per 100 μg MSNs)	–		–	8.2	9.5	14.1	–	9.8
μg EVs left (per 100 μg MSNs)	–		–	1.1	3.2	18.9	–	2.6

organic material, which became progressively denser and thicker as the amount of EVs increased, confirming the appropriate coating of the nanoparticles.

The success of the coating procedure was also confirmed by Z-Potential measurements that evidenced a switch in the surface charge from the positive value of amino-functionalized MSNs to negative values close to that of pristine EVs after coating (Fig. 1B and Table 1). The size distribution of the samples was analyzed by DLS technique, showing the presence of a narrow peak centered at approximately 150 nm for both uncoated MSNs and MSNs coated with the three ratios (Fig. 1C and Table 1). MSNs–EVsGB[3:1] sample showed also the appearance of a small population at hydrodynamic diameters greater than 1 μm, suggesting an aggregation phenomena. This could be related to an excess of EVs that may interfere with the homogenous coating, leading instead to aggregates of nanoparticles and EVs.

Even though some EVs could be smaller than MSNs, as observed in Fig. 1, the fusion mechanism favored by the application of vigorous shaking leaded to the adsorption, deformation and adhesion of the negatively charged vesicles to the positively charged silica surface. This mechanism has been already proposed in the literature for the coating of artificial nanoparticles with biological membranes [29–31].

The coating efficiency was quantitatively evaluated using a colorimetric assay for protein quantification, which is commonly used to estimate EVs amount [32]. The micrograms of proteins present in the pellets and supernatants obtained by centrifugation at the end of the coating process were determined. Since the centrifugal speed used was not sufficient to sediment pristine vesicles, the amount of EVs measured in the pellet were considered associated with the silica surface to form the coating layer. As reported in Table 1, increasing amount of proteins were found associated with the MSNs as the initial quantity of EVs increased, from MSNs:EVs ratios of 10:1 to 3:1, consistently with TEM measurements. Considering the EVs remaining in the supernatants, ratios 10:1 and 7.5:1 showed small amount of residual vesicles, while for ratio 3:1 more than 50 % of the EVs remained in solution. According to these results, increasing the EVs beyond a certain amount did not provide an improvement in coating efficiency, probably because the vesicles were no longer able to interact directly with the MSN surface. In agreement with the threshold found, the 7.5:1 was selected as the optimal ratio because it displayed the largest amount of EV associated per 100 μg of MSNs (9.5 μg versus 8.2 μg in 10:1 ratio) and the lowest amount of EVs wasted (3.2 μg versus 18.9 μg in 3:1 ratio). The selected ratio allowed to obtain homogenously coated and well-dispersed MSNs, while reducing the loss of non-associated EVs.

Consequently, the 7.5:1 MSNs:EVs ratio was used to coat MSNs with EVs derived from HeLa cells and MSNs–EVsHeLa[7.5:1] sample was fully characterized obtaining analogous results to these reported for

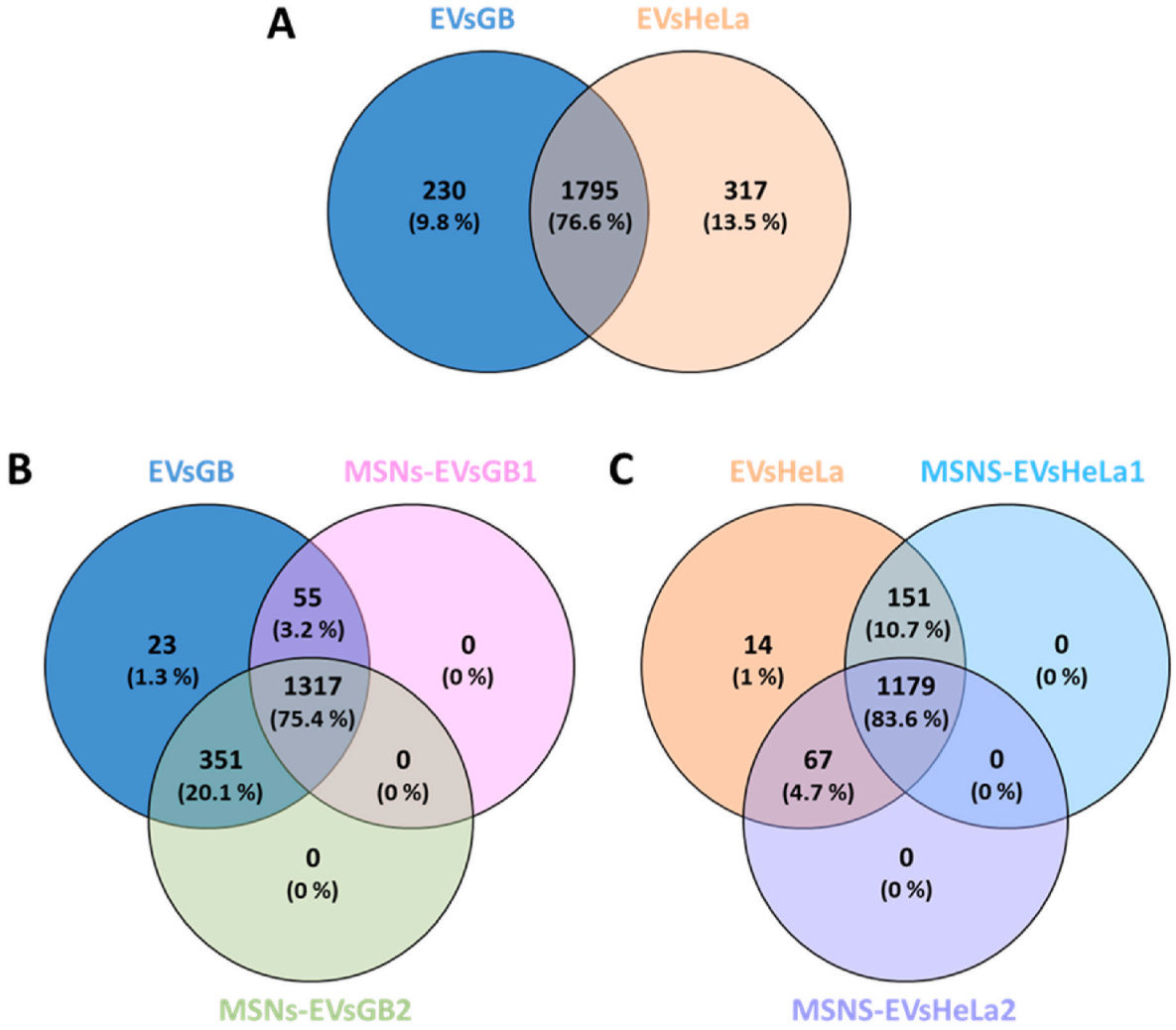

Fig. 2. Venn diagram showing the distribution of overlapping and unique proteins identified by mass spectrometry. **(A)** Total proteins found in EVs extracted from HeLa and GB are indicated by two circles; common subsets are indicated within the diagram, where most of the proteins identified in the EVs from the two cell lines are overlapping. Comparison between proteins present in extracted EVs and proteins found in two independent coatings were analyzed for **(B)** GB and **(C)** HeLa. Only proteins identified with high confidence (FDR <0.01) were considered.

EVsGB (see Fig. 1A, B and C and Table 1).

In summary, coating conditions were optimized by maximizing the combination between artificial MSNs and biological material, achieving efficient coating with EVs derived from two different cell sources.

Proteomic characterization of pristine EVs and EVs coatings. After verifying the optimal coating ratio, the next objective was to check whether the proteins present in EVs from HeLa and HGUE-GB-39 cell lines were still present in the coatings. Therefore, proteomic analysis of the proteins found in the vesicles extracted from HeLa and GB cells and those present after the MSNs coating was performed.

Proteomic analysis identified a total of 2025 proteins present in EVs or coatings from glioblastoma and 2112 proteins in the case of HeLa. On the one hand, when comparing HeLa and glioblastoma EVs, 1795 proteins common to both cell lines were detected, while 230 proteins were unique to glioblastoma and 317 unique to HeLa (Fig. 2A). On the other hand, proteins present in the EVs and in their respective coatings were compared. For this analysis, proteins not found in pristine EVs were removed and 1746 proteins were identified in glioblastoma EVs, of which 1317 proteins (75.4 %) were preserved in both MSNs-GB coated samples. Comparing each coating individually, 1372 proteins (78.6 %) were maintained in the first sample (MSNs-GB1) compared to EVs from GB, while 1668 proteins (95.5 %) were maintained in the second sample (MSNs-GB2) compared to the same EVs (Fig. 2B). As for the HeLa cell line, 1411 proteins present in HeLa EVs were identified, of which 1179 proteins (83.6 %) were maintained in both coatings. Comparing these coatings individually, 1330 proteins (94.3 %) were maintained in the first coating (MSNs-HeLa1) compared to the source EVs, while 1246 proteins (88.3 %) were identified in the second coating (MSNs-HeLa2) (Fig. 2C).

Of all the proteins identified, the most abundant in the extracted EVs and in the GB and HeLa coatings are shown in Table 2.

Among all the most abundant proteins in both EVs, several proteins stand out, such as the Neuroblast differentiation-associated protein AHNAK (AHNAK), which allows cells to produce and release vesicles that cause disruption of the stroma by surrounding fibroblasts [33]. Also, the cytoplasmic dynein 1 (DYNC1H1), which acts as a motor of intracellular vesicle motility [34] and Actin-binding protein (ACTN4) associated with aggressiveness, invasion and metastasis in certain tumors [35].

In addition, other proteins less abundant than those shown in Table 2, but also significant, were the EV-associated tetraspanins CD9, CD63 and CD81 which were found in both EVs and membrane coated MSNs of both cell lines. These tetraspanins are known to be among the major components of EVs [36].

Ultimately, proteomic analysis showed that all coatings retained at least 78.6 % of the total proteins present in the original EVs. This data allowed to confirm that a high number of proteins found in the EVs were maintained in the coatings. The *in vitro* biological behavior of optimized formulations was further analyzed to evaluate the preservation and transfer of EV properties to hybrid nanosystems, which is crucial for their effective applications.

Evaluation of the biocompatibility of uncoated and EVs-coated MSNs. The biocompatibility of the developed nanosystems was evaluated through cell viability, reactive oxygen species (ROS) and cell cycle studies. The nanoparticle effect was evaluated in the two cancerous cells lines from which EVs were derived (HeLa and HGUE-GB-39 cells) and in a healthy (non-cancerous) pre-osteoblastic cell line (MC3T3-E1 cells). Cells were seeded in 12-well plates and treated with different concentrations of uncoated MSNs and coated MSNs-EVGB and MSNs-EVsHeLa for 3 h.

Fig. 3A–C shows the cell viability in response to the three nanosystems. The uncoated MSNs were not toxic at any concentration in any of the three selected cell lines, in agreement with the literature [37]. Similarly, MSNs coated with EVs from HGUE-GB-39 or HeLa cells were not cytotoxic in the pre-osteoblastic cell line, causing only a slight decrease in cell viability when increasing concentrations. Similarly, MSNs–EVs only slightly affected the cell viability of the non-parent cancer cell line, while a significant inhibition of proliferation was observed when administrated to the respective EV source cells at the highest dose tested. This might suggest an enhanced interaction of coated nanosystems with the parent cells, as it will be thoroughly investigated by internalization studies. As it will be presented below, MSNs coated with EVs have been observed to favor cell internalization in cell lines from which the EVs are derived. Therefore, the increased cell internalization would lead to a high accumulation of MSNs in the cytoplasm that might cause cell viability to be lower than the control, as shown in Fig. 3. In fact, the reduction of the cell viability as the evaluated concentration was increased might validate this observation. Based on these results, a maximum dose of 50 μg/mL was used in all the subsequent *in vitro* assays, ensuring suitable cell viability in all cell lines evaluated.

A study of ROS was performed as part of biocompatibility tests, since nanoparticles tend to produce large amounts of reactive oxygen species that can destroy the membrane structure and lead to apoptosis, mutagenesis or necrosis [38]. The intracellular ROS content of HeLa or HGUE-GB-39 cells after stimulation with different concentration (10, 25 and 50 μg/mL) of the nanosystems for 3 h showed no significant differences with respect to control cells (Figs. S2A and C, Figs. S5A and S6A). This result confirms that these nanoparticles, whether coated with EVs or not, did not affect cell viability after exposure, in agreement with previous experiment.

Biocompatibility tests were completed with the evaluation of cell

Table 2
Proteomic analysis of the most abundant proteins in EVs and coatings originating from **(A)** HGUE-GB-39 or **(B)** HeLa. Large numbers of peptide spectrum matches (PSMs) to each protein in each of the samples are shown.

A	EVs from HGUE-GB-39			
Accession	Protein name	PSMs Evs GB	PSMs MSNS-GB1	PSMs MSNS-GB2
Q09666	Neuroblast differentiation-associated protein AHNAK (AHNAK)	160	58	183
P35579	Myosin-9 (MYH9)	133	116	144
P21333	Filamin-A (FLNA)	95	99	105
Q14204	Cytoplasmic dynein 1 heavy chain 1 (DYNC1H1)	81	98	96
Q9Y490	Talin-1 (TLN1)	82	71	86
Q00610	Clathrin heavy chain 1 (CLTC)	79	60	93
Q15149	Plectin (PLEC)	95	7	129
O75369	Filamin-B (FLNB)	80	55	91
P60709	Actin, cytoplasmic 1 (ACTB)	68	73	77
P46940	Ras GTPase-activating-like protein IQGAP1 (IQGAP1)	77	57	79
B	**EVs from HeLa**			
Accession	Protein name	PSMs EVs HeLa	PSMs MSNS-HeLa1	PSMs MSNS-HaLa2
P35579	Myosin-9 (MYH9)	83	123	165
Q09666	Neuroblast differentiation-associated protein AHNAK (AHNAK)	35	73	217
P21333	Filamin-A (FLNA)	92	99	105
Q14204	Cytoplasmic dynein 1 heavy chain 1 (DYNC1H1)	62	113	93
Q9Y490	Talin-1 (TLN1)	72	82	82
P60709	Actin, cytoplasmic 1 (ACTB)	60	86	80
O75369	Filamin-B (FLNB)	33	56	115
Q00610	Clathrin heavy chain 1 (CLTC)	52	58	75
P46940	Ras GTPase-activating-like protein IQGAP1 (IQGAP)	35	66	78
O43707	Alpha-actinin-4 (ACTN4)	45	55	70

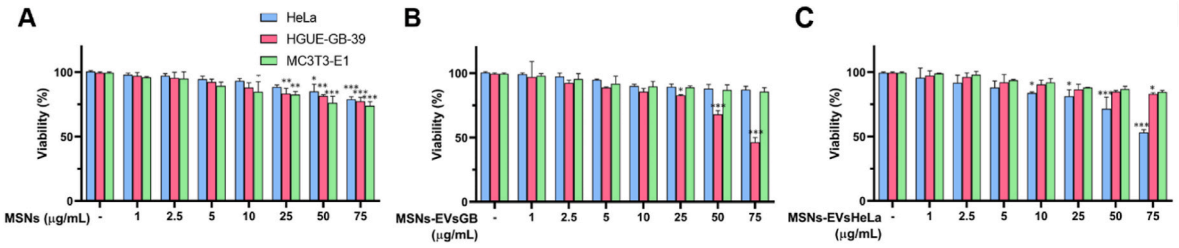

Fig. 3. Cell viability of HeLa, HGUE-GB-39 and MC3T3-E1 cells exposed to different concentrations (1, 2.5, 5, 10, 25, 50 and 75 μg/mL) of (**A**) MSNs, (**B**) MSNs–EVsGB and (**C**) MSNs–EVsHeLa for 3h. Data are means ± SD of three independent experiments. Statistical significance: *P < 0.05; ***P < 0.01; ***P < 0.001, compared with untreated controls (−).

cycle of HeLa and HGUE-GB-39 cells after being exposed to different concentrations of the developed nanocarriers (Figs. S2B and D, Figs. S7A and S8A). It was found that both nanoparticles, coated or uncoated, did not significantly alter the cell cycle, confirming the correct cell functioning and, consequently, their biocompatibility.

These *in vitro* tests have all confirmed the biocompatibility of both coated and uncoated MSNs here developed using different cell lines, which is of capital importance in the perspective of future biomedical applications of EVs-coated MSNs.

Enhanced uptake of EVs-coated MSNs by parent cancer cells. Cellular uptake of uncoated and EVs-coated MSNs was evaluated by flow cytometry in the three different cell lines. The results shown in Fig. 4A–C represent the percentages of total cell population that have internalized the different nanosystems. Uncoated MSNs (Fig. 4A) presented similar internalization rate in all cell lines, with nearly 30 % of all cells tested showing unspecific internalization of uncoated nanoparticles. In contrast, MSNs coated with both types of EVs showed increased levels of uptake in the cell line from which vesicles were derived with very marked shifts compared to the untreated cell baseline signal, as shown by representative flow cytometry histograms in Fig. S3. Namely, MSNs–EVsGB were internalized in higher extent by glioblastoma cells while MSNs–EVsHeLa by HeLa cells, both achieving nearly 100 % of internalization for concentrations of 10 μg/mL or higher (Fig. 4B and C, respectively).

The preferential internalization of coated MSNs was also supported by cell mean fluorescence intensities, which allowed to quantify the amount of nanoparticles taken up by cells (Fig. 4D–F). As for internalization percentages, an unspecific uptake was observed for uncoated MSNs. However, a marked increase in the amount of MSNs internalized by HeLa and glioblastoma cells when coated with their respective EVs was observed. The increase of fluorescence intensity was clearly dose-dependent, and the very large amounts of MSNs-EVs internalized at high doses could explain the reduction in cell viability previously observed for coated nanosystems. In this regard it has been previously reported that nanoparticle-induced cytotoxicity can be directly correlated with high cell uptake and critical amounts of accumulated MSNs in the cytoplasm were found to affect cell viability [39]. For this reason, cells exposed to uncoated MSNs that had a maximum internalization of 30 % (Fig. 4A) had a higher percentage of viability (Fig. 3A) than cells that internalized a higher percentage of MSNs-EVs (Fig. 4B and C), in which viability was lower (Fig. 3B and C).

Confocal microscopy qualitatively confirmed flow cytometry results. As shown in Fig. 4G, similar amount of uncoated MSNs was non-specifically internalized by all cell types. However, a greater amount of MSNs–EVsHeLa was observed in the cytoplasmatic perinuclear region of HeLa cells, whereas their internalization in HGUE-GB-39 and MC3T3-E1 cell lines appeared reduced. Similar results were obtained for MSNs–EVsGB, which showed preferential accumulation in glioblastoma cells, again demonstrating the selectivity of the hybrid nanosystems over the EVs coating source cells.

Different experiments have demonstrated that MSNs coated with EVs preferentially internalize in those cell lines from which vesicles were extracted. Considering that uncoated MSNs presented similar internalization rates independently of the cell line investigated, the specificity shown by MSNs-EVs nanosystems should be attributed to the vesicle coating. In this regard, the homing capabilities of tumor EVs toward parent cells have been previously reported [26,40]. Therefore, the molecular composition and protein profile of those EVs would provide the coated nanosystems with selective interaction capabilities, which might be of great interest for future targeted and personalized treatments.

Preferential barrier penetration of EV-coated MSNs in presence of parent cancer cells. The analysis of the interaction between coated and uncoated MSNs with different cells was further deepened by assessing the ability of the nanosystems to reach target cells overcoming a barrier using an *in vitro* model previously reported in the literature [18]. Cells were seeded in a well and nanoparticles were located on top of a transwell that was set in the well (Fig. 5A). The passage of the nanosystems through the transwell membrane and their internalization in target cell was evaluated.

The amount of green-labeled MSNs that were able to cross the transwell membrane and reach the cultured cells was visualized by fluorescence microscopy after 24 h of incubation. As shown in Fig. 5B, larger amounts of translocated nanoparticles (green spots) were observed for MSNs–EVsGB and MSNs–EVsHeLa samples than for uncoated MSNs, and specifically when exposed to HGUE-GB-39 or HeLa cells, respectively. The images indicated a preferential penetration of coated nanosystems toward EV parent cells, reinforcing the previously observed internalization results.

This qualitative observation was confirmed by the quantification of the nanosystems above, inside and below the transwell (Fig. 5C–E). In this sense, the media above and below the transwell membrane were collected and analyzed, and then the polycarbonate membrane was dissolved to quantify the amount of MSNs eventually absorbed into it.

It is important to notice that when MSNs, both coated or uncoated, were placed into the transwell with no cells seeded in the bottom of the well (basal control), almost all nanoparticles remained in the transwell insert. This is indicative that the nanosystems did not passively diffuse through the membrane but cells must be there to somehow attract the nanoparticles towards them. In this regard, when exposed to the respective EV source cells, the two coated nanosystems showed a significant decrease in the percentages of MSNs remaining above the transwell membrane (Fig. 5C), with less than 20 % MSNs–EVs left. In contrast, small or no decrease of MSNs with respect to basal control were observed for MSNs–EVs exposed to non-parental cell lines and for uncoated MSNs in all the three cell lines. Moreover, the minimal percentages of MSNs detected after the dissolution confirmed that the nanoparticles were not retained inside the transwell membrane (Fig. 5D). More interestingly, the low percentages measured in the medium collected below the membrane (Fig. 5E) indicated that those MSNs that have crossed the transwell did not remain in the liquid but were rather internalized by recipient cells.

Taken together, these results showed that coated nanosystems were able to actively target their parent cells and avoid non-specific transport towards other cell types. The tendency of tumor-derived EVs to

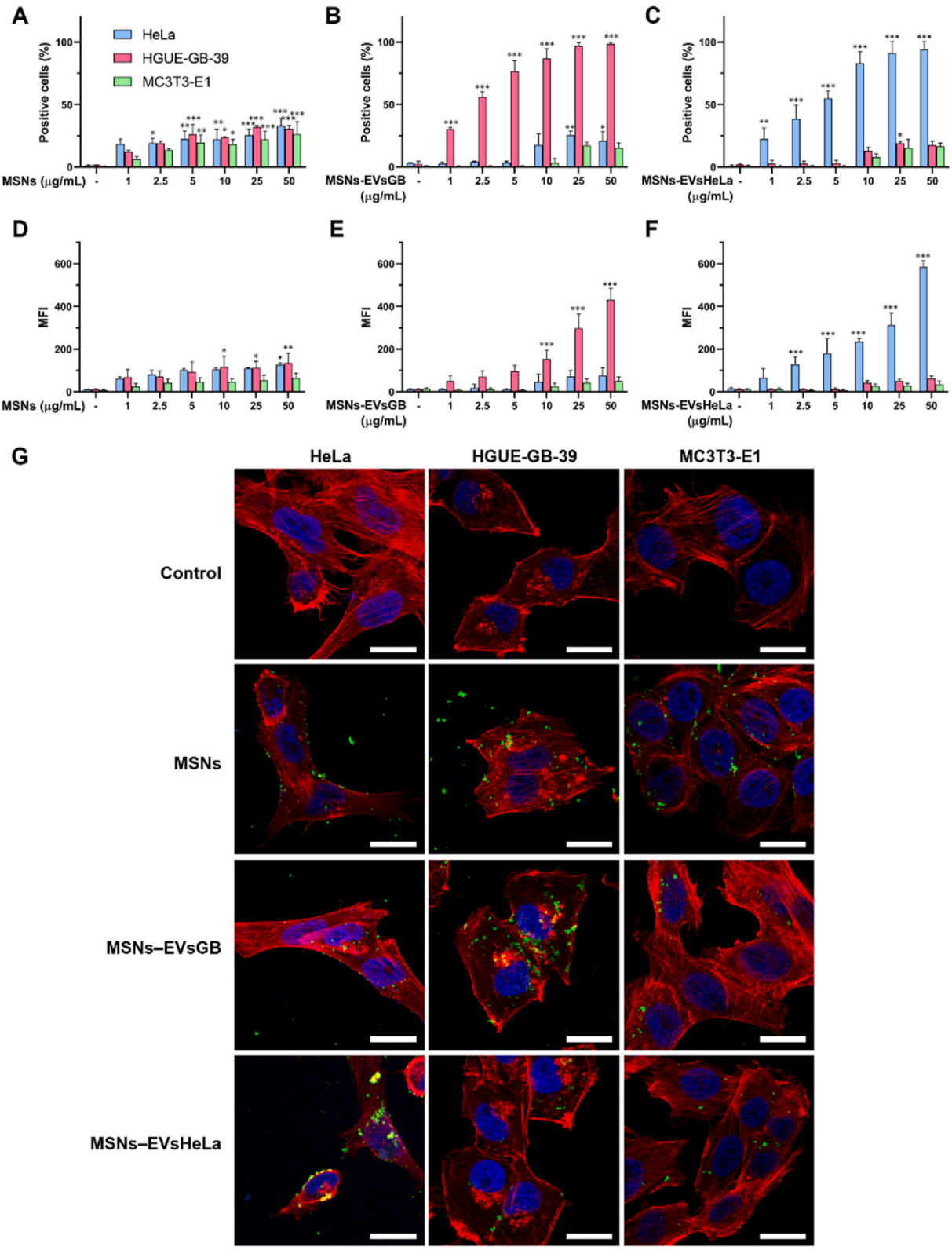

Fig. 4. Cellular internalization of uncoated and EVs-coated MSNs in HeLa, HGUE-GB-39 and MC3T3-E1 cells by flow-cytometry and confocal microscopy. Flow cytometry results are reported as percentages of positive cells and mean fluorescence intensities (MFI) of cells treated with different concentrations (1, 2.5, 5, 10, 25 and 50 μg/mL) of FITC-labeled (**A, D**) MSNs, (**B, E**) MSNs–EVsGB and (**C, F**) MSNs–EVsHeLa for 3 h. Data are means ± SD of three independent experiments. Statistical significance: *$P < 0.05$; **$P < 0.01$; ***$P < 0.001$, compared with untreated controls (−). (**G**) Representative confocal laser scanning microscopy images of HeLa (left column), HGUE-GB-39 (central column) and MC3-T3-E1 (right column) cells incubated with uncoated MSNs and coated MSNs–EVsGB and MSNs–EVsHeLa for 3 h. Cell membranes were labeled with phalloidin (red), nuclei with DAPI (blue) and MSNs with FITC (green). Scale bars: 20 μm. (For interpretation of the references to color in this figure legend, the reader is referred to the Web version of this article.)

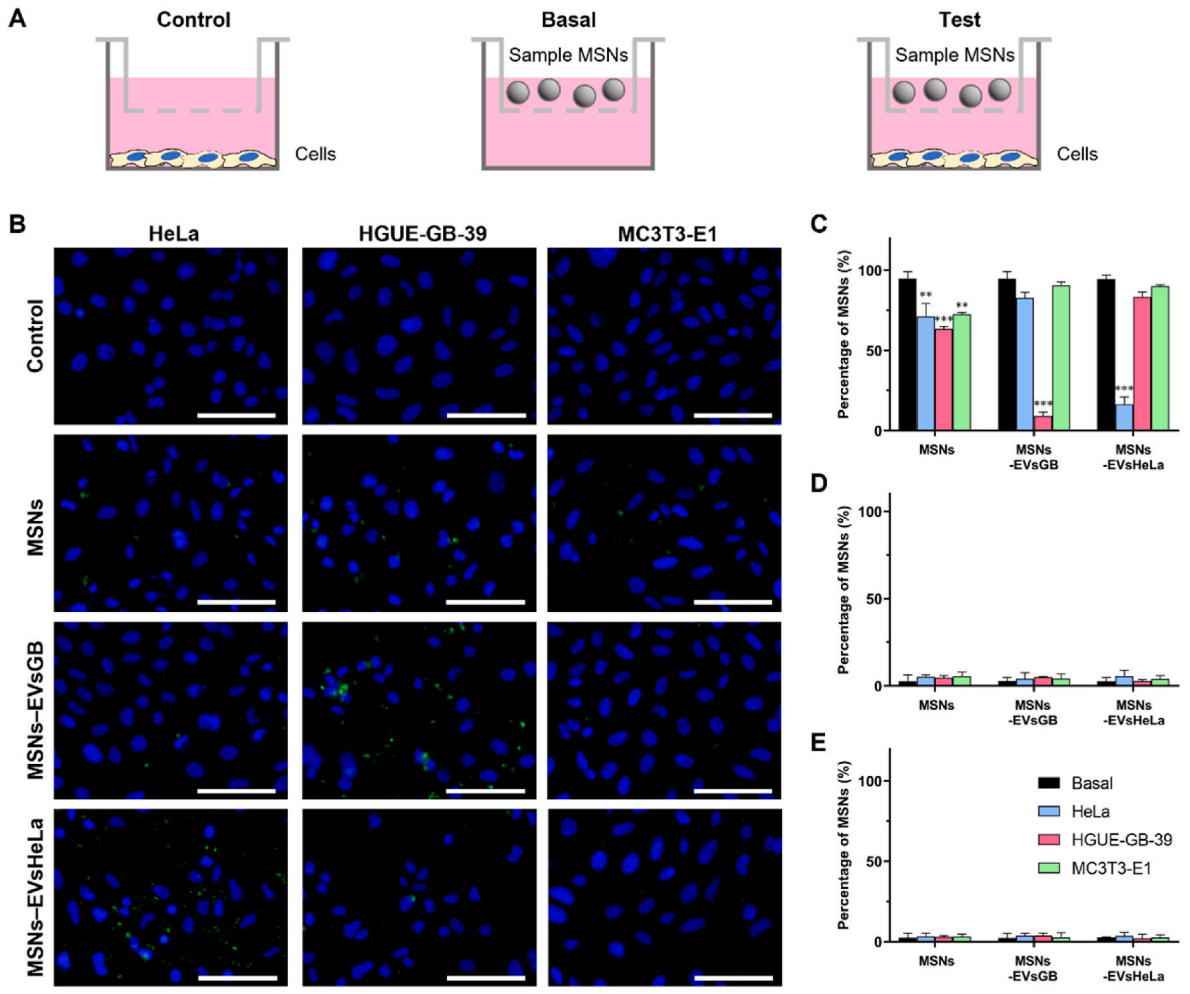

Fig. 5. *In vitro* transwell assay. (**A**) Schematic representation of experiment setup. (**B**) Fluorescence microscopy images of MSNs, MSNs–EVsGB and MSNs–EVsHeLa passed through transwell membrane and internalized by HeLa (left column), HGUE-GB-39 (central column) and MC3T3-E1 (right column) cells after 24 h exposure. Cell nuclei were labeled with DAPI (blue) and MSNs with FITC (green). Scale bars: 100 μm. Quantification of the percentages of residual nanosystems (**C**) above, (**D**) inside and (**E**) below the transwell membrane. Data are means ± SD of three independent experiments. Statistical significance: $^{**}P < 0.01$; $^{***}P < 0.001$, compared with the respective basal control without cells. (For interpretation of the references to color in this figure legend, the reader is referred to the Web version of this article.)

recognize and preferentially accumulate in particular cells or tissues is well described in literature [26,41], and this preliminary *in vitro* model suggested that the EV tropism capabilities were efficiently transferred to the EVs-coated MSNs which was one of the aims of the present work.

Effect of EV coating on uptake and intracellular drug release from MSNs. After evaluating the enhanced internalization and migration towards specific cancer cells, the delivery performances of the nanosystems were evaluated.

To this end, doxorubicin (DOX), a common antitumoral drug, was used as drug model because its fluorescence properties allowed to follow its accumulation and intracellular release. The elevated surface area and pore volume of synthesized MSNs ensured a high loading capacity, 2.1 μmolDOX/mgMSNs, in agreement with the literature [8]. Loaded MSNs@DOX were coated with EVs following the previously optimized procedure, obtaining drug loaded hybrid nanosystems (MSNs@DOX–EVsGB and MSNs@DOX–EVsHeLa) and the delivery and therapeutic efficacy in targeted cancer cells were evaluated *in vitro*.

As expected, the enhanced internalization of EVs-coated nanoparticles in the cell lines from which vesicles were derived resulted in a preferential accumulation of the drug, as shown by flow cytometry results in Fig. 6A–C.

Evaluation of the percentages of DOX internalization did not lead to relevant conclusion, since nearly 100 % of positive cells were found for all tested conditions (data not shown), likely due to the broad fluorescence spectrum of DOX. However, different histogram peak shifts were clearly observed (Fig. S4) and when considering mean fluorescence intensities appreciable differences were found. The DOX internalization mediated by the nanocarriers was observed to depend on the EVs-coated carrier and the cell types evaluated, in line with the internalization observed for nanosystems without drug. As shown in Fig. 6B and C, mean intensities of HGUE-GB-39 and HeLa cells related to DOX red fluorescence showed a significant increase when cells were treated with MSNs@DOX–EVsGB and MSNs@DOX–EVsHeLa, respectively. Compared to uncoated MSNs@DOX, 7-fold higher intensities were observed for all the concentrations tested, which again highlight the selective internalization of EVs-coated MSNs. Moreover, no significant internalization of DOX was observed when coated MSNs were administered to non-parent cell lines, in line with the previously observed internalization results.

Confocal microscopy allowed to directly visualize the uptake and intracellular distribution of the drug (Fig. 6D). After 3 h incubation, DOX fluorescence was observed inside the nuclei and in the surrounding nuclear regions of both cancer cells and pre-osteoblastic cells treated with the uncoated MSNs@DOX, presumably due to their unspecific cellular internalization. However, drug uptake was even higher in the two cancer cell lines treated with the nanosystems coated with their

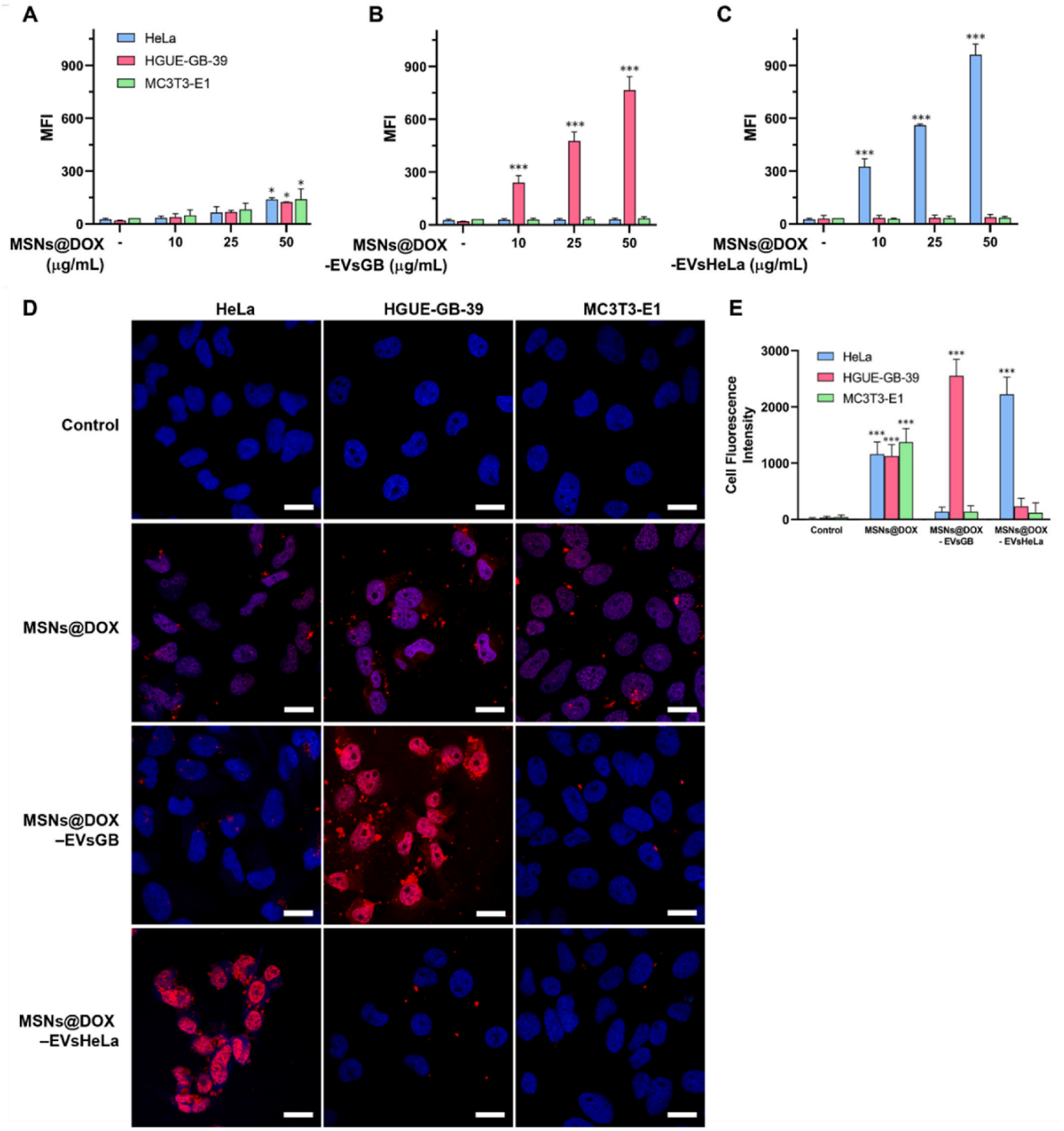

Fig. 6. Evaluation of uptake and intracellular release of DOX from uncoated and EV-coated MSNs. Mean intensities related to DOX red fluorescence of HeLa, HGUE-GB-39 and MC3T3-E1 cells treated with different concentrations (10, 25 and 50 μg/mL) of loaded (**A**) MSNs@DOX, (**B**) MSNs@DOX–EVsGB and (**C**) MSNs@DOX–EVsHeLa for 3 h. Data are means ± SD of three independent experiments. Statistical significance: *$P < 0.05$; ***$P < 0.001$, compared with untreated controls (−). (**D**) Representative confocal laser scanning microscopy images of HeLa (left column), HGUE-GB-39 (central column) and MC3T3-E1 (right column) cells incubated with MSNs@DOX, MSNs@DOX–EVsGB or MSNs@DOX–EVsHeLa for 3 h. Cell nuclei were labeled with DAPI (blue) and DOX was visualized in the red channel. Scale bars: 20 μm. (**E**) Mean fluorescence intensity of DOX inside the cells obtained by quantification of different confocal images Statistical significance: ***$P < 0.001$, compared with untreated controls. (For interpretation of the references to color in this figure legend, the reader is referred to the Web version of this article.)

respective EVs, as evidenced by the values of intracellular mean fluorescence intensity obtained by quantification of different images (Fig. 6E).

Interestingly, almost no red fluorescence was observed when MSNs@DOX–EVs were administrated to non-parent cells. This can certainly be attributed to the low interaction of coated nanosystems with cell types other than the source cells, but also suggested that EV coating may prevent extracellular leakage of DOX, which could then enter into cells *via* passive diffusion [42]. Likely, the EV layer observed around the MSNs covering the open-pore silica structure (Fig. 1A) was able to provide a barrier against premature drug release, supporting the efficiency of the developed coating method. In contrast, when internalization in target parent cells occurred, a spread red fluorescence overlapping with the blue fluorescence of DAPI staining was observed. This revealed the typical accumulation of DOX in the cell nuclei, indicating that the drug was efficiently released by the coated nanosystems once inside the cells.

Both flow cytometry and confocal microscopy showed that EVs-coated MSNs provided a selective accumulation and efficient delivery of the drug in specific cells, showing great potential as targeted drug delivery systems.

Therapeutic potential of EVs–coated MSNs. The therapeutic potential of the proposed nanosystems was evaluated studying their *in vitro* antitumor activity. Cell viability, ROS and cell cycle analyses of cells treated with 10, 25 and 50 μg/mL of DOX loaded nanosystems were performed.

Cell viability was assessed at 3, 6 and 24 h to monitor how the DOX released from both uncoated and EV-coated MSNs affected the different cell lines overtime. Fig. 7A, B and C show that uncoated DOX-loaded MSNs presented significant decrease in cell viability, although there was only a 30 % cell death after 24 h in the three cell lines. Pristine MSNs were not toxic at these concentrations (as observed in Fig. 3A), thus this effect could be reasonably attributed to the previously found unspecific internalization of uncoated MSNs in all cell lines, which was *ca.* 30 %. Once internalized, DOX was released from MSNs intracellularly causing the 30 % cell death after 24 h.

However, when MSNs were loaded with DOX and coated with EVs derived from glioblastoma or HeLa cells, different cytotoxic response were observed depending on the cell line. On the one hand, Fig. 7D–F shows the effect of DOX when the different cells were exposed to different concentrations of MSNS@DOX-EVsGB. When exposed to HGUE-GB-39 cells, a high cell death (up to 90 % after 24 h) was observed in a dose dependent manner. However, when exposed to the other two cell lines, the decrease in viability was even lower than that observed for uncoated MSNs. Therefore, the EVs coating might somehow be removed or destabilized during uptake process uncovering the pore entrances from the silica nanoparticles. This coating removal might trigger the doxorubicin release, which would explain the cell viability reduction as nanoparticle internalization increase. Again, this is in agreement with the fact the EVs-coated MSNs are better internalized, and therefore DOX released, in the cell lines from which vesicles were derived.

Fig. 7G–I, revealed the same trend for MSNs@DOX-EVsHeLa and a high cell death (95 %) was observed in HeLa cells, while almost no cell death was found for the other two cell lines. These results supported what observed by confocal microscopy, as the higher internalization and specific release of DOX in parent cancer cells by coated nanosystems resulted in an enhanced and selective cytotoxic effect compared to uncoated MSNs.

To understand the mechanism of cell death, ROS and cell cycle analyses were performed on the two cancer cell lines. With respect to ROS

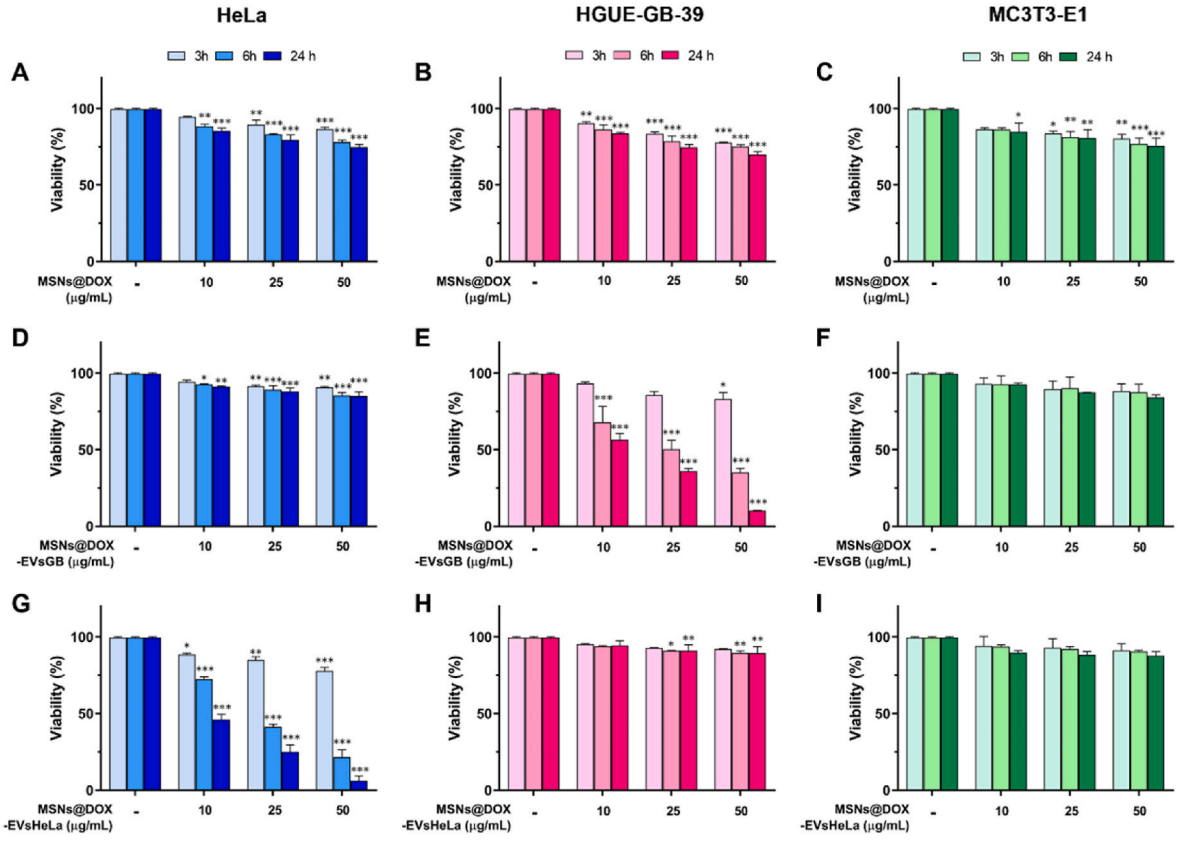

Fig. 7. Cell viability in different cell lines with different nanosystems. HeLa, HGUE-GB-39 and MC3T3-E1 cells were incubated with (**A**, **B**, **C**) MSNs@DOX, (**D**, **E**, **F**) MSNs@DOX–EVsGB and (**G**, **H**, **I**) MSNs@DOX–EVsHeLa at different concentrations (10, 25, 50 μg/mL) for 3h and evaluated at 3, 6 and 24 h. After these times, viability was tested on all samples. Cells cultured without MSNs were used as control (−). Data are means ± SD of three independent experiments. Statistical significance: *P < 0.05; **P < 0.01; ***P < 0.001, compared with untreated controls (−).

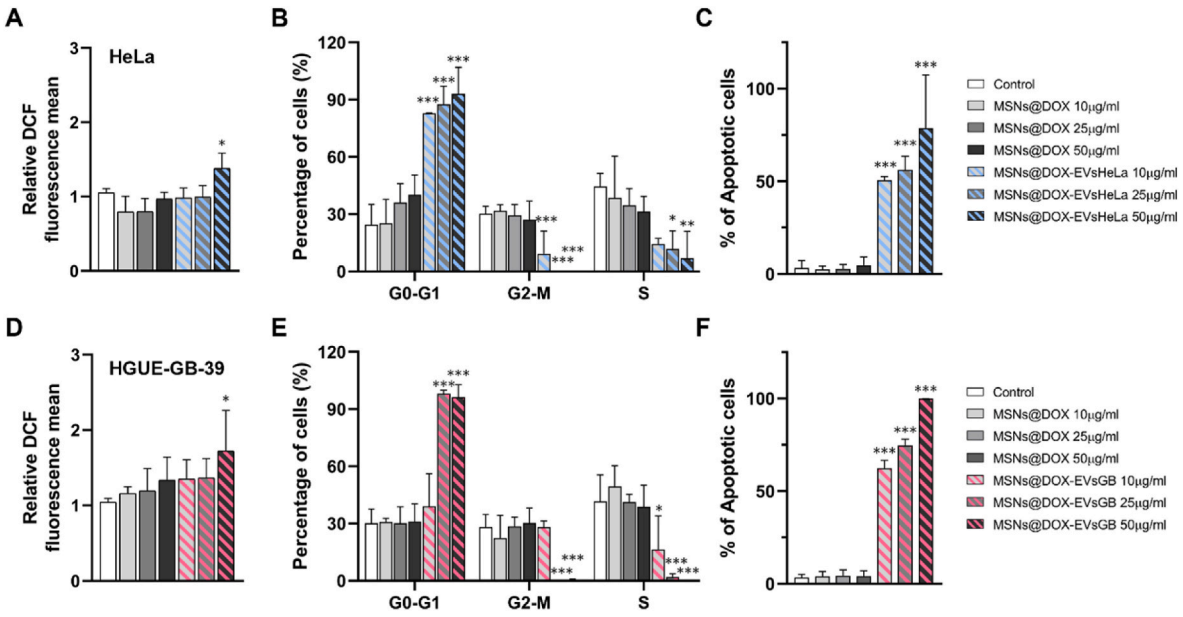

Fig. 8. Effects of MSNs@DOX and MSNs@DOX-EVs on ROS and cell cycle. Hela and HGUE-GB-39 cells were exposed to coated and uncoated MSNs at different concentrations (10, 25 and 50 μg/mL) for 3 h and then analyzed. (**A, D**) Measurement of ROS production expressed as mean fluorescence intensity obtained by flow cytometry. (**B, E**) Percentages of cells in G0-G1, G2-M and S phase of cell cycle and (**C, F**) percentages of apoptotic cells of HeLa and HGUE-GB-39 cells, respectively, analyzed by flow cytometry. Data are means ± SD of three independent experiments. Statistical significance: *P < 0.05; **P < 0.01; ***P < 0.001, compared with untreated controls (white bars).

(Fig. 8A and D, Figs. S5B and S6B), when both cell lines (HeLa and HGUE-GB-39) were respectively exposed to uncoated MSNs@DOX, they showed no significant changes. Nevertheless, when these two cell types were treated with MSNs@DOX coated with EVs from their parent line (HeLa and HGUE-GB-39), they presented significant increase in ROS content at the dose of 50 μg/mL compared to uncoated MSNs, confirming the enhanced delivery of DOX by coated nanosystems.

Analyses of the cell cycle of both cancer cell lines revealed similar results (Fig. 8B and E, Figs. S7B and S8B). There were no significant changes in HeLa or HGUE-GB-39 cells when exposed to uncoated MSNs. However, the cell cycle was arrested in the G0/G1 phase by coated nanosystems. In both cell lines, the percentages of cells in G0/G1 phase increased at increasing concentrations of MSNs@DOX-EVs, with a consequent decrease of other phases. In addition, high percentages of apoptosis were observed when cells were treated with coated nanosystems, reaching 50 % even at the lowest concentration of 10 μg/mL (Fig. 8C and F). Literature studies report G1 and G2 cell cycle arrest and eventual induction of apoptosis as mechanisms for DOX action [43]. Therefore these results confirmed that the high DOX release from EV-coated nanosystems exposed for 3 h to the different cell lines was responsible for the cytotoxicity observed in Fig. 7E and G. This relationship is possible since previous studies have shown that doxorubicin encapsulated in tumor cell exosomes exhibited higher cytotoxicity against these parental cells than the free drug [44,45].

2. Conclusions

In this work, we have developed novel bioinspired nanosystems based on MSNs coated with tumor derived EVs, leveraging the benefits of inorganic silica core and biologically derived coating material. The EV coating strategy was found to remarkably enhance the uptake of nanocarriers in specific parent cells, even in presence of a model barrier, highlighting its potential for the formulation of targeted nanoplatforms. As a result, EVs-coated nanosystems demonstrated a selective therapeutic potential, showing preferential accumulation and drug release only upon internalization in targeted cancer cells which resulted in specific cytotoxicity.

Here doxorubicin was used as drug model, but the simple tailoring of MSNs as nanocarriers could guarantee the implementation of the proposed nanosystems for the delivery of different kind of therapeutic agents, alone or in synergistic combination. The use of EVs extracted from two different cancer cells lines, both ensuring promising therapeutic outcomes in the specific parent cells, proved a great level of selectivity toward specific cell population. Moreover, it also indicated the good versatility of the proposed coating strategy. In future perspectives, EVs-coated MSNs could be adapted for the treatment of different types of cancer or other pathologies by selecting the appropriate source cells for vesicle isolation, even up to the use of autologous EVs collected from patient blood or tissues to create fully biocompatible delivery systems for personalized nanomedicine applications.

3. Methods

Materials. Chemicals: Cetyltrimethylammonium bromide (CTAB), tetraethyl orthosilicate (TEOS), Rhodamine B isothiocyanate, fluorescein isothiocyanate (FITC), ammonium nitrate, sodium hydroxide, toluene, absolute ethanol and phosphotungstic acid were purchased from Sigma-Aldrich. 3-Aminopropyltriethoxysilane (APTES) and doxorubicin hydrochloride were purchased from ABCR GmbH & Co. KG. Dimethyl sulfoxide (DMSO) was acquired from PanReac. All the above chemicals were used as received without further purification. The deionized water was purified using a Milli-Q Advantage A-10 purification system (Millipore Corporation) to a final resistivity of 18.2 MΩcm.

Reagents for *in vitro* assays: Triton X-100, bovine serum albumin (BSA), paraformaldehyde, Trypan Blue (TB), propidium iodide (PI), phalloidin-Atto 565, fluoroshield™ with DAPI and Dulbecco's Modified Eagle Medium: Nutrient Mixture F-12 (DMEM/F12) were purchased from Sigma-Aldrich. Alpha modified Eagle's medium (α-MEM), Dulbecco's Modified Eagle Medium (DMEM), fetal bovine serum (FBS), L-glutamine and Phosphate-buffered saline (PBS) solution were purchased from Gibco. Penicillin/streptomycin (13–0050) was bought from ZellShield. Alamar blue reagent, Sytox™ Green nucleic acid stain, 2′,7′-dichlorofluorescein diacetate (DCF H/DA) and microBCA Protein Assay Kit were purchased from Thermo Fisher Scientific.

Synthesis and surface functionalization of MSNs. Mesoporous silica nanoparticles were synthesized by a modification of Stöber method [27] using CTAB as structure directing agent. First, 1 g of CTAB was dissolved in 480 mL of water and 3.5 mL of NaOH 2 M in a round bottom flask and heated at 80 °C under magnetic stirring. After 30 min, 5 mL of TEOS were added dropwise using an automated syringe pump (flow rate 0.33 mL/min) and the resulting synthesis mixture was maintained at 80 °C for 2 h. Then, the solution was centrifuged at 17,000 g for 15 min and washed once with water and twice with ethanol.

MSNs labeled with rhodamine B ($\lambda_{Ex/Em}$ = 543/580 nm) or fluorescein ($\lambda_{Ex/Em}$ = 492/520 nm) were obtained by incorporating the dye in the silica structure. Briefly, 1 mg of rhodamine B-isothiocyanate or fluorescein-isothiocyanate (FITC) was dissolved into 100 μL of ethanol and reacted with 2.2 μL of APTES for 2 h. Then, the dye solution was mixed with TEOS just before the injection and the reaction was carried out as described above.

MSNs surface was functionalized with $-NH_2$ groups, using 3-Aminopropyltriethoxysilane (APTES). The desired amount of MSNs was dried under vacuum at room temperature for 5 h and then redispersed in dry toluene by magnetic stirring under nitrogen gas flow. After 10 min, a solution of dry toluene containing an amount of APTES corresponding to 10 % wt of MSNs was added. The mixture was heated at 80 °C and kept overnight under continuous stirring under inert atmosphere. In order to remove unbound APTES molecules, functionalized MSNs were centrifuged at 17,000 g for 15 min and washed once with toluene and twice with ethanol.

Finally, CTAB was removed by ionic exchange using ammonium nitrate. In details, MSNs were redispersed in 350 mL of ammonium nitrate solution (10 mg/mL in 95 % ethanol) and kept overnight at 80 °C under vigorous magnetic stirring. Then, the nanoparticles were centrifuged at 17,000 g for 15 min and washed once with water and twice with ethanol. A second CTAB removal step was performed and the final product was dried at 70 °C overnight.

Extraction of extracellular vesicles. Extracellular vesicles were isolated from conditioned media of HeLa and HGUE-GB-39 cells. HeLa and HGUE-GB-39 cells were cultured in DMEM and DMEM/F-12, respectively, supplemented with 10 % FBS, 1 % penicillin/streptomycin and 2 mM L-glutamine under atmospheric conditions of 5 % CO_2 and 95 % humidity at 37 °C. When they reached 80 % confluency, the medium was removed, cells were washed with PBS and fresh medium supplemented with 10 % EVs-depleted FBS, 2 mM L-glutamine and 1 % penicillin/streptomycin was added. To obtain depleted FBS, FBS was centrifuged overnight at 100,000 g at 4 °C using a XL-90 Ultracentrifuge equipped with a 70Ti fixed-angle rotor (Beckman Coulter). After 48 h of culturing, conditioned media were collected and processed to isolate EVs according to a differential ultracentrifugation protocol [46].

In detail, the collected cell culture media were centrifuged at 300 g at 4 °C for 10 min. Supernatants were recovered and centrifuged at 2000 g at 4 °C for 20 min. Then, supernatants were transferred in ultracentrifuge polycarbonate bottles and ultracentrifuged at 10,000 g at 4 °C for 30 min. Supernatants were collected again and ultracentrifuged at 100,000 g at 4 °C for 70 min. Finally, a washing step was performed by resuspending the obtained pellet containing the EVs in cold PBS and ultracentrifuging further at 100,000 g at 4 °C for 60 min. PBS was discarded and purified EVs were resuspended in 300 μL of cold PBS, aliquoted and stored at −80 °C for further use.

The yield of each isolation was quantified by measuring the protein content of purified EVs by micro BCA protein assay using bovine serum albumin standards as references. Aliquots of 50 μL of EVs were diluted 1:10 in PBS and processed according to manufacturer instructions. All samples were analyzed in triplicate and the absorbance at 562 nm was measured with a Synergy 4 multimode plate reader (Biotek Instruments).

MSNs coating with extracellular vesicles. MSNs coated with EVs isolated from HeLa or HGUE-GB-39 cells were obtained by co-incubating the two components in a 1:1 (v/v) solution of deionized water and PBS. Different ratio (expressed as μg of MSNs: μg of EVs protein) were tested, and namely 10:1, 7.5:1 and 3:1.

Amino functionalized MSNs were resuspended in deionized water at concentration of 1 mg/mL and redispersed by sonicating for 10 min. Redispersed nanoparticles were added to an equivalent volume of PBS containing the desired amount of EVs and the mixture was incubated under orbital shaking (200 rpm) at 37*C for 1.5 h. In order to remove the EVs not associated with silica surface, the samples were centrifuged at 10,000 g for 15 min.

Physicochemical characterization. Amino-functionalized MSNs were analyzed by X-ray diffraction (XRD) to evaluate the order of mesopores using a Philips X-Pert MPD diffractometer equipped with Cu-Kα radiation. Surface area and pore size distribution were measured by nitrogen adsorption using a Micromeritics ASAP 2010 sorptometer. The surface area was calculated with Brunauer-Emmett-Teller (BET) method [47] and the pore size distribution with Barrett–Joyner–Halenda (BJH) method from the isotherm desorption branch [48]. The surface composition of MSNs was analyzed by Fourier Transformed Infrared (FT-IR) spectroscopy using a Nicolet Nexus spectrometer (Thermo Fisher Scientific).

EVs derived from HeLa and HGUE-GB-39 cells, uncoated MSNs and MSNs coated with EVs (MSNs–EVsHeLa and MSNs–EVsGB) were analyzed by transmission electron microscopy (TEM) using a JEOL JEM 1400 electron microscope operated at 200 kV and equipped with a charge-coupled device (CCD) camera (KeenView Camera). A drop of sample was deposited on a copper grid, 200 mesh, coated with amorphous carbon film and stained with a solution of 1 % phosphotungstic acid (PTA) solution in water. Hydrodynamic size distribution and Z-Potential were measured with a Zetasizer Nano ZS (Malvern Instruments) equipped with a 633 nm laser. EVs were analyzed in PBS while MSNs and MSNs coated with EVs in a 1:1 (v/v) solution of deionized water and PBS.

To quantify the amount of EVs associated with the silica surface, supernatants collected after the coating step and the corresponding MSNs–EVs samples were analyzed with micro BCA protein assay. Samples were properly diluted in PBS to meet the concentration working range of the kit and processed according to manufacturer instructions. All samples were analyzed in duplicate and absorbance at 562 nm was measured.

Proteomics analysis of EVs and EVs-coated MSNs. The protocol employed in the characterization of proteins present in EVs and MSNs coating by proteomics followed the subsequent steps:

Sample preparation: To each sample tube 5 times its volume of cold acetone was added and incubated overnight at −20 °C. The next day the acetone was removed by centrifuging the sample and discarding the supernatant.

Digestion with the Preomics iST kit: The precipitated sample was treated with 50 μl of LYSE buffer for 10 min at 95 °C, transferred to the columns and 50 μl of DIGEST solution was added. After 2 h at 37 °C, 100 μl of STOP buffer was added, shaken, and centrifuged for 2 min at 3800 g. The digest was washed, first with 100 μl WASH1 buffer (centrifuge 2 min at 3800 g) and then with 100 μl WASH 2 (centrifuge 2 min at 3800 g) and eluted with 100 μl ELUTE twice. The sample was dried in speed-vac and reconstituted in 10 μl LC-LOAD. The concentration of peptides in the digest was measured on the Qubit fluorimeter.

Separation of peptides by reversed-phase chromatography: From the digested peptide mixture, about 500 ng were injected into the Vanquish Neo nano-HPLC (Thermo), concentrated on a PEPMAP100C18 Nano-Viper Trap precolumn (Thermo Fisher) and separated on a 50 cm PEPMAP RSLC C18 column (Thermo) with a gradient of 5 %–35 % acetonitrile, 0.1 % formic acid in 90 min before introduction for analysis in the mass spectrometer.

Analysis by DDA (shotgun): Peptides separated by chromatography were electrospray ionized in positive mode and analyzed on a Q Exactive HF mass spectrometer (Thermo) in DDA (data dependent acquisition) mode. From each MS scan (between 350 and 1500 Da) the 10 most

intense precursors (charge between 2+ and 5+) were selected for HCD (high collision energy dissociation) fragmentation and the corresponding MS/MS spectra were acquired.

Protein identification by shotgun: The data files generated in the shotgun analysis were transferred to the Proteome Discoverer software (Thermo), where the identification of PSMs (peptide-spectrum matches) of each MS/MS spectrum was performed by comparison with the theoretical mass lists corresponding to the mass of the precursor of origin, extracted from the database of human proteins collected in the Uniprot sequence repository, using the Sequest search engine. The peptides thus identified were assigned to their corresponding proteins. When a peptide can be assigned to several proteins, the software uses the principle of parsimony to generate a "Master" protein reported in the results. The percolator algorithm was used to estimate the FDR (false positive rate) and filtered by a q value < 0.01 for proteins identified with high confidence. At the same time the search in a database of common contaminants was performed. The proteins thus identified were discarded from the results.

Drug loading. Doxorubicin hydrochloride (DOX) was used as drug model thanks to its fluorescence properties. For the preparation of loaded MSNs (MSNs@DOX), 10 mg of amino-functionalized nanoparticles were added to 2.5 mL of DOX solution (0.01 M in PBS) and kept under vigorous stirring at room temperature overnight. Then, MSNs@DOX were centrifuged at 7426 g for 15 min, thoroughly washed with PBS to remove unloaded drug and dried in vacuum at 37 °C for 2 h. The solutions from each washing step were collected to measure the drug loading capacity. The amount of loaded DOX was calculated as difference between the initial amount and the drug left in the supernatants, quantified by UV–Vis measurements at wavelength of 480 nm.

Cell culture. Three cell lines were used for the performance of all experiments. HeLa and HGUE-GB-39 cells were maintained as mentioned above. MC3T3-E1 cells were cultured in α-MEM supplemented with 10 % FBS, 1 % penicillin/streptomycin and 2 mM L-glutamine under atmospheric conditions of 5 % CO_2 and 95 % humidity at 37 °C.

To perform the *in vitro* experiments, cells were cultured for 24 h before being exposed to the different nanosystems.

Cell uptake and confocal microscopy assay. For internalization assays, HeLa, HGUE-GB-39 and MC3T3-E1 cell lines were seeded in 6-well plates (1×10^6 cell/well). On the one hand, different concentrations of fluorescein-labeled coated and uncoated MSNs (1, 2.5, 5, 10, 25 and 50 μg/mL of MSNs, MSNs-EVsHeLa or MSNs-EvsGB) were tested. On the other hand, different concentrations of doxorubicin-loaded coated and uncoated MSNs (10, 25, 50 μg/mL of MSNs@DOX, MSNs@DOX-EVsHeLa or MSNs@DOX-EVsGB). In both experiments, treatments were left for 3 h at 37 °C and 5 % CO_2. After this time, the cells were harvested and centrifuged at 966 g for 5 min at 15 °C. The pellets were resuspended in 250 μl of PBS and kept on ice in dark until the time of measurement. A FACSCalibur flow cytometer (Becton Dickinson) was used for the analysis, detecting the fluorescence of FITC and DOX, respectively. Results are expressed in term of mean fluorescence intensity (MFI) and percentage of cells that had internalized the nanosystems, calculated as the number of fluorescence-positive cells divided by the number of live cells. Untreated cells were used as negative control. Data are the mean ± SD of three independent assays.

For confocal microscopy assays, cells were exposed to a single representative concentration of coated and uncoated MSNs labeled with fluorescein (50 μg/mL) or DOX (25 μg/mL) for 3 h. Cells were then washed with 1X PBS and fixed with 4 % paraformaldehyde in PBS (w/v) at 37 °C for 20 min. Next, the cells were washed with 1X PBS and permeabilized with Triton X-100 for 5 min at 4 °C. Finally, cells exposed to the FITC-labeled nanosystems were stained with phalloidin (10 μL in 1 mL of 1X PBS) and DAPI (3 μM in 1X PBS) for 20 min and 5 min, respectively. Cells exposed to the DOX-loaded nanosystems were stained exclusively with DAPI. Images were acquired with a FV1200 laser scanning microscope (Olympus).

Cell proliferation assay. Cell viability was assessed by the Alamar blue method. The three cell lines were seeded in 12-well plates (10,000 cell/well). After 24 h incubation, the cells were exposed to different concentrations of the different nanosystems. On the one hand, in a first experiment, nanoparticle concentrations of 1, 2.5, 5, 10, 25, 50 or 75 μg/mL of MSNs, MSNs-EVsHeLa or MSNs-EVsGB were used. On the other hand, in a second experiment, nanoparticle concentrations of 10, 25 and 50 μg/mL of MSNs-DOX, MSNs@DOX-EVsHeLa or MSNs@DOX-EVsGB were employed. In both assays, the nanosystems were left in contact with the cells for 3h at 37 °C. After this time, the cells were washed with PBS and a 1:10 solution of Alamar Blue reagent was added in fresh medium and cells were incubated for 4h in the absence of light, according to the manufacturer instructions. Then, fluorescence was quantified using a Synergy 4 multimode plate reader with excitation at 560 nm and emission at 590 nm wavelengths. The first assay was measured exclusively after an exposure time to the nanosystems of 3h while the viability of cells treated with DOX-loaded nanosystems was evaluated at 3h, 6h and 24h. Data are mean ± SD of three independent cultures.

Transwell assay. Polycarbonate membrane inserts (Costar) of 3 μm pore size were used in 24-well plates to study the penetration ability of EVs-coated and uncoated MSNs toward the three cell lines. 50 μg of FITC-labeled MSNs, MSNs-EVsHeLa or MSNs-EVsGB resuspended in 200 μl of culture medium were added on top of the inserts while 20,000 cells/mL of each cell line were seeded in the bottom wells. A well filled with the medium corresponding to each cell line was used as a negative control. After 24 h, the medium from the top and the bottom of polycarbonate membrane was collected and MSNs were quantified by a Biotek Synergy 4 microplate reader (excitation/emission: 490/520 nm). The membrane was dissolved in DMSO and the fluorescence of the solution was also measured to calculate the amount of MSNs retained inside the membrane. DAPI was used to stain the nuclei of cells attached to the well. A fluorescence microscope with a 20x objective was used to visualize the translocated MSNs internalized by the cells (four individual fields per well).

Intracellular reactive oxygen species (ROS) production. The tumor cell lines, HeLa and HGUE-GB-39, were seeded in 6-well plates (1×10^6 cell/well). After 24 h, cells were exposed to coated and uncoated Rhodamine B-labeled MSNs (MSNs, MSNs-EVsHeLa or MSNs-EVsGB) or DOX-loaded coated and uncoated MSNs, MSNs@DOX, MSNs@DOX-EVsHeLa or MSNs@DOX-EVsGB) at concentrations of 10, 25 and 50 μg/mL. After 3 h, cells were harvested and incubated with 100 mM 2′,7′-dichlorofluorescein diacetate (DCFH/DA) at 37 °C for 30 min to determine ROS production. A FACSCalibur flow cytometer was used to measure DCF fluorescence. Data are the mean ± SD of three independent experiments.

Cell cycle analysis. HeLa and HGUE-GB-39 cells were seeded and treated with unloaded or DOX loaded nanosystems with same experimental conditions used for ROS analysis. After 3 h, the cells were collected, washed with PBS and 700 μl of ice-cold absolute ethanol were added dropwise while vortexing. Samples were left overnight at 4 °C. The next day, 700 μl of PBS was added and samples were centrifuged at 1315 g for 5 min. The samples were then washed with PBS and pellets were resuspended in a mixture containing 100 μg/mL RNase and 50 μg/mL PI or Sytox Green in PBS for cells treated with unloaded or DOX-loaded MSNs, respectively. The samples were then incubated under orbital shaking for 3 h in the absence of light and at room temperature. Finally, the analysis of PI or Sytox Green fluorescence was performed by flow cytometer. Data represent the mean ± SD of three independent assays.

Statistical analysis. *In vitro* data were interpreted as mean ± SD. Statistical significance was calculated by two-tailed unpaired Student's t-test where $P < 0.05$ was estimated significant. Confocal images were quantified with the Fiji program (Image J). Statistical analyses of cellular results were prepared with Graphpad Prism (Graphpad software).

4. Associated content

Supporting **Information.** Physicochemical characterization of amino functionalized MSNs, ROS content and cell cycle of HeLa and HGUE-GB-39 cells exposed to the nanosystems without DOX and representative dot plots and histograms of all flow cytometry analysis. This material is available free of charge at http://pubs.acs.org.

Credit author statement

Conceptualization: MVR, MM; Investigation: BD, CJJ; Methodology: BD, CJJ; Funding acquisition: MVR, MM; Project administration: MVR, MM; Writing – original draft: BD, CJJ, MM; Writing – review & editing: all authors. All authors read and approved the final manuscript.

Declaration of competing interest

The authors declare that they have no known competing financial interests or personal relationships that could have appeared to influence the work reported in this paper.

Data availability

Data will be made available on request.

Acknowledgment

This work was supported by the Spanish "Ministerio de Ciencia e Innovación" through the project PID2019-106436RB-I00 (Agencia Estatal de Investigación, AEI/10.13039/501100011033); EUROPEAN RESEARCH COUNCIL, ERC-2015-AdG (VERDI), grant No. 694160; and Fondo Europeo de Desarrollo Regional (FEDER), CM-React Anticipa-UCM (PR38/21-21). We acknowledge the support from the "(MAD2D-CM)-UCM" project funded by Comunidad de Madrid, by the Recovery, Transformation and Resilience Plan, and by NextGenerationEU from the European Union (Ref: PR47/21-MAD2D-CM).

Appendix A. Supplementary data

Supplementary data to this article can be found online at https://doi.org/10.1016/j.mtbio.2023.100850.

References

[1] J. Wolfram, M. Ferrari, Clinical cancer nanomedicine, Nano Today 25 (2019) 85–98, https://doi.org/10.1016/j.nantod.2019.02.005.
[2] E. Blanco, H. Shen, M. Ferrari, Principles of nanoparticle design for overcoming biological barriers to drug delivery, Nat. Biotechnol. 33 (2015) 941–951, https://doi.org/10.1038/nbt.3330.
[3] S. Mura, J. Nicolas, P. Couvreur, Stimuli-responsive nanocarriers for drug delivery, Nat. Mater. 12 (2013) 991–1003, https://doi.org/10.1038/nmat3776.
[4] M.J. Mitchell, M.M. Billingsley, R.M. Haley, M.E. Wechsler, N.A. Peppas, R. Langer, Engineering precision nanoparticles for drug delivery, Nat. Rev. Drug Discov. 20 (2021) 101–124, https://doi.org/10.1038/s41573-020-0090-8.
[5] N.L. Klyachko, C.J. Arzt, S.M. Li, O.A. Gololobova, E. V Batrakova, Extracellular vesicle-based therapeutics: preclinical and clinical investigations, Pharmaceutics 12 (2020), https://doi.org/10.3390/pharmaceutics12121171.
[6] V. Chugh, K. Vijaya Krishna, A. Pandit, Cell membrane-coated mimics: a methodological approach for fabrication, characterization for therapeutic applications, and challenges for clinical translation, ACS Nano 15 (2021) 17080–17123, https://doi.org/10.1021/acsnano.1c03800.
[7] Y. Liu, J. Luo, X. Chen, W. Liu, T. Chen, Cell membrane coating technology: a promising strategy for biomedical applications, Nano-Micro Lett. 11 (2019) 100, https://doi.org/10.1007/s40820-019-0330-9.
[8] M. Manzano, M. Vallet-Regí, Mesoporous silica nanoparticles for drug delivery, Adv. Funct. Mater. 30 (2020), 1902634, https://doi.org/10.1002/adfm.201902634.
[9] M. Vallet-Regí, F. Schüth, D. Lozano, M. Colilla, M. Manzano, Engineering mesoporous silica nanoparticles for drug delivery: where are we after two decades? Chem. Soc. Rev. 51 (2022) 5365–5451, https://doi.org/10.1039/d1cs00659b.
[10] M. Manzano, M. Vallet-Regí, Mesoporous silica nanoparticles in nanomedicine applications, J. Mater. Sci. Mater. Med. 29 (2018) 65, https://doi.org/10.1007/s10856-018-6069-x.
[11] T.-P. Liu, S.-H. Wu, Y.-P. Chen, C.-M. Chou, C.-T. Chen, Biosafety evaluations of well-dispersed mesoporous silica nanoparticles: towards in vivo-relevant conditions, Nanoscale 7 (2015) 6471–6480, https://doi.org/10.1039/C4NR07421A.
[12] M. Manzano, M. Vallet-Regí, New developments in ordered mesoporous materials for drug delivery, J. Mater. Chem. 20 (2010) 5593, https://doi.org/10.1039/b922651f.
[13] M. Gisbert-Garzarán, D. Lozano, K. Matsumoto, A. Komatsu, M. Manzano, F. Tamanoi, M. Vallet-Regí, Designing mesoporous silica nanoparticles to overcome biological barriers by incorporating targeting and endosomal escape, ACS Appl. Mater. Interfaces 13 (2021) 9656–9666, https://doi.org/10.1021/acsami.0c21507.
[14] C. Jiménez-Jiménez, M. Manzano, M. Vallet-Regí, Nanoparticles coated with cell membranes for biomedical applications, Biology 9 (2020) 406, https://doi.org/10.3390/biology9110406.
[15] J. Zhang, Y. Miao, W. Ni, H. Xiao, J. Zhang, Cancer cell membrane coated silica nanoparticles loaded with ICG for tumour specific photothermal therapy of osteosarcoma, Artif. Cells, Nanomed. Biotechnol. 47 (2019) 2298–2305, https://doi.org/10.1080/21691401.2019.1622554.
[16] M. Xuan, J. Shao, L. Dai, Q. He, J. Li, Macrophage cell membrane camouflaged mesoporous silica nanocapsules for in vivo cancer therapy, Adv. Healthcare Mater. 4 (2015) 1645–1652, https://doi.org/10.1002/adhm.201500129.
[17] M. Xuan, J. Shao, J. Zhao, Q. Li, L. Dai, J. Li, Magnetic mesoporous silica nanoparticles cloaked by red blood cell membranes: applications in cancer therapy, Angew. Chem. Int. Ed. 57 (2018) 6049–6053, https://doi.org/10.1002/anie.201712996.
[18] C. Jiménez-Jiménez, A. Moreno-Borrallo, B. Dumontel, M. Manzano, M. Vallet-Regí, Biomimetic camouflaged nanoparticles with selective cellular internalization and migration competences, Acta Biomater. 157 (2023) 395–407, https://doi.org/10.1016/j.actbio.2022.11.059.
[19] W. Lei, C. Yang, Y. Wu, G. Ru, X. He, X. Tong, S. Wang, Nanocarriers surface engineered with cell membranes for cancer targeted chemotherapy, J. Nanobiotechnol. 20 (2022) 45, https://doi.org/10.1186/s12951-022-01251-w.
[20] Y. Liao, Y. Zhang, N.T. Blum, J. Lin, P. Huang, Biomimetic hybrid membrane-based nanoplatforms: synthesis, properties and biomedical applications, Nanoscale Horizons 5 (2020) 1293–1302, https://doi.org/10.1039/D0NH00267D.
[21] H. Liu, Y.-Y. Su, X.-C. Jiang, J.-Q. Gao, Cell membrane-coated nanoparticles: a novel multifunctional biomimetic drug delivery system, Drug Deliv. Transl. Res. 13 (2023) 716–737, https://doi.org/10.1007/s13346-022-01252-0.
[22] R. Kalluri, V.S. LeBleu, The biology, function, and biomedical applications of exosomes, Science 367 (2020), https://doi.org/10.1126/science.aau6977.
[23] C. Liu, W. Zhang, Y. Li, J. Chang, F. Tian, F. Zhao, Y. Ma, J. Sun, Microfluidic sonication to assemble exosome membrane-coated nanoparticles for immune evasion-mediated targeting, Nano Lett. 19 (2019) 7836–7844, https://doi.org/10.1021/acs.nanolett.9b02841.
[24] A. Hoshino, B. Costa-Silva, T.L. Shen, G. Rodrigues, A. Hashimoto, M. Tesic Mark, H. Molina, S. Kohsaka, A. Di Giannatale, S. Ceder, S. Singh, C. Williams, N. Soplop, K. Uryu, L. Pharmer, T. King, L. Bojmar, A.E. Davies, Y. Ararso, T. Zhang, H. Zhang, J. Hernandez, J.M. Weiss, V.D. Dumont-Cole, K. Kramer, L.H. Wexler, A. Narendran, G.K. Schwartz, J.H. Healey, P. Sandstrom, K. Jørgen Labori, E. H. Kure, P.M. Grandgenett, M.A. Hollingsworth, M. De Sousa, S. Kaur, M. Jain, K. Mallya, S.K. Batra, W.R. Jarnagin, M.S. Brady, O. Fodstad, V. Muller, K. Pantel, A.J. Minn, M.J. Bissell, B.A. Garcia, Y. Kang, V.K. Rajasekhar, C.M. Ghajar, I. Matei, H. Peinado, J. Bromberg, D. Lyden, Tumour exosome integrins determine organotropic metastasis, Nature (2015), https://doi.org/10.1038/nature15756.
[25] V. Du Nguyen, H.Y. Kim, Y.H. Choi, J.-O. Park, E. Choi, Tumor-derived extracellular vesicles for the active targeting and effective treatment of colorectal tumors in vivo, Drug Deliv. 29 (2022) 2621–2631, https://doi.org/10.1080/10717544.2022.2105444.
[26] L. Qiao, S. Hu, K. Huang, T. Su, Z. Li, A. Vandergriff, J. Cores, P.U. Dinh, T. Allen, D. Shen, H. Liang, Y. Li, K. Cheng, Tumor cell-derived exosomes home to their cells of origin and can be used as Trojan horses to deliver cancer drugs, Theranostics (2020), https://doi.org/10.7150/thno.39434.
[27] Q. Cai, Z.-S. Luo, W.-Q. Pang, Y.-W. Fan, X.-H. Chen, F.-Z. Cui, Dilute solution routes to various controllable morphologies of MCM-41 silica with a basic medium, Chem. Mater. 13 (2001) 258–263, https://doi.org/10.1021/cm990661z.
[28] G. Midekessa, K. Godakumara, J. Ord, J. Viil, F. Lättekivi, K. Dissanayake, S. Kopanchuk, A. Rinken, A. Andronowska, S. Bhattacharjee, T. Rinken, A. Fazeli, Zeta potential of extracellular vesicles: toward understanding the attributes that determine colloidal stability, ACS Omega 5 (2020) 16701–16710, https://doi.org/10.1021/acsomega.0c01582.
[29] B. Illes, P. Hirschle, S. Barnert, V. Cauda, S. Wuttke, H. Engelke, Exosome-coated metal–organic framework nanoparticles: an efficient drug delivery platform, Chem. Mater. 29 (2017) 8042–8046, https://doi.org/10.1021/acs.chemmater.7b02358.
[30] S. Mornet, O. Lambert, E. Duguet, A. Brisson, The formation of supported lipid bilayers on silica nanoparticles revealed by cryoelectron microscopy, Nano Lett. (2005), https://doi.org/10.1021/nl048153y.
[31] P.N. Durfee, Y.S. Lin, D.R. Dunphy, A.J. Muñiz, K.S. Butler, K.R. Humphrey, A. J. Lokke, J.O. Agola, S.S. Chou, I.M. Chen, W. Wharton, J.L. Townson, C. L. Willman, C.J. Brinker, Mesoporous silica nanoparticle-supported lipid bilayers (protocells) for active targeting and delivery to individual Leukemia cells, ACS Nano (2016), https://doi.org/10.1021/acsnano.6b02819.

[32] C. Théry, K.W. Witwer, E. Aikawa, M.J. Alcaraz, J.D. Anderson, R. Andriantsitohaina, A. Antoniou, T. Arab, F. Archer, G.K. Atkin-Smith, D.C. Ayre, J.M. Bach, D. Bachurski, H. Baharvand, L. Balaj, S. Baldacchino, N.N. Bauer, A. A. Baxter, M. Bebawy, C. Beckham, A. Bedina Zavec, A. Benmoussa, A.C. Berardi, P. Bergese, E. Bielska, C. Blenkiron, S. Bobis-Wozowicz, E. Boilard, W. Boireau, A. Bongiovanni, F.E. Borràs, S. Bosch, C.M. Boulanger, X. Breakefield, A.M. Breglio, M. Brennan, D.R. Brigstock, A. Brisson, M.L.D. Broekman, J.F. Bromberg, P. Bryl-Górecka, S. Buch, A.H. Buck, D. Burger, S. Busatto, D. Buschmann, B. Bussolati, E. I. Buzás, J.B. Byrd, G. Camussi, D.R.F. Carter, S. Caruso, L.W. Chamley, Y.T. Chang, A.D. Chaudhuri, C. Chen, S. Chen, L. Cheng, A.R. Chin, A. Clayton, S.P. Clerici, A. Cocks, E. Cocucci, R.J. Coffey, A. Cordeiro-da-Silva, Y. Couch, F.A.W. Coumans, B. Coyle, R. Crescitelli, M.F. Criado, C. D'Souza-Schorey, S. Das, P. de Candia, E. F. De Santana, O. De Wever, H.A. del Portillo, T. Demaret, S. Deville, A. Devitt, B. Dhondt, D. Di Vizio, L.C. Dieterich, V. Dolo, A.P. Dominguez Rubio, M. Dominici, M.R. Dourado, T.A.P. Driedonks, F.V. Duarte, H.M. Duncan, R. M. Eichenberger, K. Ekström, S. EL Andaloussi, C. Elie-Caille, U. Erdbrügger, J. M. Falcón-Pérez, F. Fatima, J.E. Fish, M. Flores-Bellver, A. Försönits, A. Frelet-Barrand, F. Fricke, G. Fuhrmann, S. Gabrielsson, A. Gámez-Valero, C. Gardiner, K. Gärtner, R. Gaudin, Y.S. Gho, B. Giebel, C. Gilbert, M. Gimona, I. Giusti, D.C. I. Goberdhan, A. Görgens, S.M. Gorski, D.W. Greening, J.C. Gross, A. Gualerzi, G. N. Gupta, D. Gustafson, A. Handberg, R.A. Haraszti, P. Harrison, H. Hegyesi, A. Hendrix, A.F. Hill, F.H. Hochberg, K.F. Hoffmann, B. Holder, H. Holthofer, B. Hosseinkhani, G. Hu, Y. Huang, V. Huber, S. Hunt, A.G.E. Ibrahim, T. Ikezu, J. M. Inal, M. Isin, A. Ivanova, H.K. Jackson, S. Jacobsen, S.M. Jay, M. Jayachandran, G. Jenster, L. Jiang, S.M. Johnson, J.C. Jones, A. Jong, T. Jovanovic-Talisman, S. Jung, R. Kalluri, S. ichi Kano, S. Kaur, Y. Kawamura, E.T. Keller, D. Khamari, E. Khomyakova, A. Khvorova, P. Kierulf, K.P. Kim, T. Kislinger, M. Klingeborn, D. J. Klinke, M. Kornek, M.M. Kosanović, Á.F. Kovács, E.M. Krämer-Albers, S. Krasemann, M. Krause, I.V. Kurochkin, G.D. Kusuma, S. Kuypers, S. Laitinen, S. M. Langevin, L.R. Languino, J. Lannigan, C. Lässer, L.C. Laurent, G. Lavieu, E. Lázaro-Ibáñez, S. Le Lay, M.S. Lee, Y.X.F. Lee, D.S. Lemos, M. Lenassi, A. Leszczynska, I.T.S. Li, K. Liao, S.F. Libregts, E. Ligeti, R. Lim, S.K. Lim, A. Linē, K. Linnemannstöns, A. Llorente, C.A. Lombard, M.J. Lorenowicz, Á.M. Lörincz, J. Lötvall, J. Lovett, M.C. Lowry, X. Loyer, Q. Lu, B. Lukomska, T.R. Lunavat, S.L. N. Maas, H. Malhi, A. Marcilla, J. Mariani, J. Mariscal, E.S. Martens-Uzunova, L. Martin-Jaular, M.C. Martinez, V.R. Martins, M. Mathieu, S. Mathivanan, M. Maugeri, L.K. McGinnis, M.J. McVey, D.G. Meckes, K.L. Meehan, I. Mertens, V. R. Minciacchi, A. Möller, M. Møller Jørgensen, A. Morales-Kastresana, J. Morhayim, F. Mullier, M. Muraca, L. Musante, V. Mussack, D.C. Muth, K. H. Myburgh, T. Najrana, M. Nawaz, I. Nazarenko, P. Nejsum, C. Neri, T. Neri, R. Nieuwland, L. Nimrichter, J.P. Nolan, E.N.M. Nolte-'t Hoen, N. Noren Hooten, L. O'Driscoll, T. O'Grady, A. O'Loghlen, T. Ochiya, M. Olivier, A. Ortiz, L.A. Ortiz, X. Osteikoetxea, O. Ostegaard, M. Ostrowski, J. Park, D.M. Pegtel, H. Peinado, F. Perut, M.W. Pfaffl, D.G. Phinney, B.C.H. Pieters, R.C. Pink, D.S. Pisetsky, E. Pogge von Strandmann, I. Polakovicova, I.K.H. Poon, B.H. Powell, I. Prada, L. Pulliam, P. Quesenberry, A. Radeghieri, R.L. Raffai, S. Raimondo, J. Rak, M. I. Ramirez, G. Raposo, M.S. Rayyan, N. Regev-Rudzki, F.L. Ricklefs, P.D. Robbins, D.D. Roberts, S.C. Rodrigues, E. Rohde, S. Rome, K.M.A. Rouschop, A. Rughetti, A. E. Russell, P. Saá, S. Sahoo, E. Salas-Huenuleo, C. Sánchez, J.A. Saugstad, M. J. Saul, R.M. Schiffelers, R. Schneider, T.H. Schøyen, A. Scott, E. Shahaj, S. Sharma, O. Shatnyeva, F. Shekari, G.V. Shelke, A.K. Shetty, K. Shiba, P.R.M. Siljander, A. M. Silva, A. Skowronek, O.L. Snyder, R.P. Soares, B.W. Sódar, C. Soekmadji, J. Sotillo, P.D. Stahl, W. Stoorvogel, S.L. Stott, E.F. Strasser, S. Swift, H. Tahara, M. Tewari, K. Timms, S. Tiwari, R. Tixeira, M. Tkach, W.S. Toh, R. Tomasini, A. C. Torrecilhas, J.P. Tosar, V. Toxavidis, L. Urbanelli, P. Vader, B.W.M. van Balkom, S.G. van der Grein, J. Van Deun, M.J.C. van Herwijnen, K. Van Keuren-Jensen, G. van Niel, M.E. van Royen, A.J. van Wijnen, M.H. Vasconcelos, I.J. Vechetti, T. D. Veit, L.J. Vella, É. Velot, F.J. Verweij, B. Vestad, J.L. Viñas, T. Visnovitz, K. V. Vukman, J. Wahlgren, D.C. Watson, M.H.M. Wauben, A. Weaver, J.P. Webber, V. Weber, A.M. Wehman, D.J. Weiss, J.A. Welsh, S. Wendt, A.M. Wheelock, Z. Wiener, L. Witte, J. Wolfram, A. Xagorari, P. Xander, J. Xu, X. Yan, M. Yáñez-Mó, H. Yin, Y. Yuana, V. Zappulli, J. Zarubova, V. Žėkas, J. ye Zhang, Z. Zhao, L. Zheng, A.R. Zheutlin, A.M. Zickler, P. Zimmermann, A.M. Zivkovic, D. Zocco, E. K. Zuba-Surma, Minimal information for studies of extracellular vesicles 2018 (MISEV2018): a position statement of the International Society for Extracellular Vesicles and update of the MISEV2014 guidelines, J. Extracell. Vesicles (2018), https://doi.org/10.1080/20013078.2018.1535750.

[33] T.A. Silva, B. Smuczek, I.C. Valadão, L.M. Dzik, R.P. Iglesia, M.C. Cruz, A. Zelanis, A.S. de Siqueira, S.M.T. Serrano, G.S. Goldberg, R.G. Jaeger, V.M. Freitas, AHNAK enables mammary carcinoma cells to produce extracellular vesicles that increase neighboring fibroblast cell motility, Oncotarget 7 (2016) 49998–50016, https://doi.org/10.18632/oncotarget.10307.

[34] X. Chu, X. Chen, Q. Wan, Z. Zheng, Q. Du, Nuclear mitotic apparatus (NuMA) interacts with and regulates astrin at the mitotic spindle, J. Biol. Chem. 291 (2016) 20055–20067, https://doi.org/10.1074/jbc.M116.724831.

[35] D. Tentler, E. Lomert, K. Novitskaya, N.A. Barlev, Role of ACTN4 in tumorigenesis, metastasis, and EMT, Cells 8 (2019), https://doi.org/10.3390/cells8111427.

[36] Y. Fan, C. Pionneau, F. Cocozza, P.-Y. Boëlle, S. Chardonnet, S. Charrin, C. Théry, P. Zimmermann, E. Rubinstein, Differential proteomics argues against a general role for CD9, CD81 or CD63 in the sorting of proteins into extracellular vesicles, J. Extracell. Vesicles 12 (2023), e12352, https://doi.org/10.1002/jev2.12352.

[37] E. Álvarez, M. Estévez, C. Jiménez-Jiménez, M. Colilla, I. Izquierdo-Barba, B. González, M. Vallet-Regí, A versatile multicomponent mesoporous silica nanosystem with dual antimicrobial and osteogenic effects, Acta Biomater. (2021), https://doi.org/10.1016/j.actbio.2021.09.027.

[38] Z. Yu, Q. Li, J. Wang, Y. Yu, Y. Wang, Q. Zhou, P. Li, Reactive oxygen species-related nanoparticle toxicity in the biomedical field, Nanoscale Res. Lett. 15 (2020) 115, https://doi.org/10.1186/s11671-020-03344-7.

[39] C.-C. Chou, W. Chen, Y. Hung, C.-Y. Mou, Molecular elucidation of biological response to mesoporous silica nanoparticles in vitro and in vivo, ACS Appl. Mater. Interfaces 9 (2017) 22235–22251, https://doi.org/10.1021/acsami.7b05359.

[40] B. Moon, S. Chang, Exosome as a delivery vehicle for cancer therapy, Cells 11 (2022), https://doi.org/10.3390/cells11030316.

[41] S.E. Emam, A.S. Abu Lila, N.E. Elsadek, H. Ando, T. Shimizu, K. Okuhira, Y. Ishima, M.A. Mahdy, F.-E.S. Ghazy, T. Ishida, Cancer cell-type tropism is one of crucial determinants for the efficient systemic delivery of cancer cell-derived exosomes to tumor tissues, Eur. J. Pharm. Biopharm. Off. J. Arbeitsgemeinschaft Fur Pharm. Verfahrenstechnik e.V. 145 (2019) 27–34, https://doi.org/10.1016/j.ejpb.2019.10.005.

[42] C. Chen, W. Sun, W. Yao, Y. Wang, H. Ying, P. Wang, Functional polymeric dialdehyde dextrin network capped mesoporous silica nanoparticles for pH/GSH dual-controlled drug release, RSC Adv. 8 (2018) 20862–20871, https://doi.org/10.1039/C8RA03163K.

[43] M. Kciuk, A. Gielecińska, S. Mujwar, D. Kołat, Ż. Kałuzińska-Kołat, I. Celik, R. Kontek, Doxorubicin-an agent with multiple mechanisms of anticancer activity, Cells 12 (2023), https://doi.org/10.3390/cells12040659.

[44] Y. Yang, Y. Chen, F. Zhang, Q. Zhao, H. Zhong, Increased anti-tumour activity by exosomes derived from doxorubicin-treated tumour cells via heat stress, Int. J. Hyperther. 31 (2015) 498–506, https://doi.org/10.3109/02656736.2015.1036384.

[45] M. Harmati, E. Gyukity-Sebestyen, G. Dobra, L. Janovak, I. Dekany, O. Saydam, E. Hunyadi-Gulyas, I. Nagy, A. Farkas, T. Pankotai, Z. Ujfaludi, P. Horvath, F. Piccinini, M. Kovacs, T. Biro, K. Buzas, Small extracellular vesicles convey the stress-induced adaptive responses of melanoma cells, Sci. Rep. 9 (2019), 15329, https://doi.org/10.1038/s41598-019-51778-6.

[46] C. Théry, S. Amigorena, G. Raposo, A. Clayton, Isolation and characterization of exosomes from cell culture supernatants and biological fluids, Curr. Protoc. Cell Biol. (2006), https://doi.org/10.1002/0471143030.cb0322s30.

[47] S. Brunauer, P.H. Emmett, E. Teller, Adsorption of gases in multimolecular layers, J. Am. Chem. Soc. 60 (1938) 309–319, https://doi.org/10.1021/ja01269a023.

[48] E.P. Barrett, L.G. Joyner, P.P. Halenda, The determination of pore volume and area distributions in porous substances. I. Computations from nitrogen isotherms, J. Am. Chem. Soc. 73 (1951) 373–380, https://doi.org/10.1021/ja01145a126.